The Pennsylvania State University
The Graduate School

STUDIES ON THE ACOUSTIC FAR-FIELD DISTANCE OF URBAN AIR MOBILITY AIRCRAFT

A Thesis in
Aerospace Engineering
by
Keon Wong Hur

Submitted in Partial Fulfillment
of the Requirements
for the Degree of

Master of Science

May 2023

The thesis of Keon Wong Hur was reviewed and approved by the following:

Kenneth S. Brentner
Professor of Aerospace Engineering
Thesis Advisor

Eric Greenwood
Assistant Professor of Aerospace Engineering

James G. Coder
Associate Professor of Aerospace Engineering

Amy R. Pritchett
Professor of Aerospace Engineering
Head of the Department of Aerospace Engineering

Abstract

The noise generation of multirotor aircraft, including urban air mobility (UAM) aircraft, must be understood to integrate these aircraft into the transportation infrastructure. In general, a far-field characterization of aircraft noise is desirable, because the measured or predicted noise can be readily generalized from one far-field distance to any other, whereas in the near field, this generalization is not applicable. Therefore, the purpose of this thesis is to provide guidance on determining the far-field distance for multirotor aircraft so that measurements are made in a far field, where acoustic pressure waves dominate the signal.

The coupled system of OpenVSP (generating the computational geometry of aircraft components), VSP2WOPWOP or CHARM (both used for computing the air loads) and PSU-WOPWOP (Ffowcs Williams-Hawkings equation for the tonal noise and Brooks, Pope, and Marcolini model for the broadband noise predictions) is used for the research. The far-field distance for an approximate S-76 model, small uncrewed aircraft systems (sUAS), and a generic electric vertical take-off and landing (eVTOL) were examined. Regarding the sUAS far field studies, the number of rotors was varied (from 1 to 4, 6, and 8: i.e., a single rotor, quadcopter, hexacopter, and octocopter) to examine its effect on the far-field distance. Proportionality between the number of rotors and far-field distance was found when the distance was normalized by the rotor diameter. In addition, the effect of vehicle size on the far-field distance was inspected to see whether changing the size of the vehicle would affect the result. To consider vehicle size,

the arm lengths of the quadcopter were varied to be 0.7, 2.1, and 3.5 rotor diameters. As in the case where the number of rotors was varied, proportionality between the vehicle size and far-field distance was found when the distance was normalized by the rotor diameter. When the distance was normalized by the vehicle diameter, it was found that far-field distance ranged from 1.5 to 2.0 vehicle diameters for all the cases in the numbers of rotors and vehicle size studies. This suggests the possibility of setting up a general rule for the far-field distance based on sUAS vehicle size.

For the generic eVTOL studies, both hover and forward flight were examined. Compared to the sUAS case, the result showed a larger value of far-field distance, 5.4 vehicle diameters, for both cases of hover and forward flight, assuming the noise source is the full vehicle. This difference is likely from multiple reasons including: different operating conditions, higher fidelity aerodynamic models, and computational procedures. This result implies that there may be additional parameters needed for a consistent rule to estimate far- field distance among different configurations of larger multicopters.

Contents

List of Figures

List of Tables

Nomenclature

Characters

Latin

$\square^2$	wave operator
c	speed of sound in the undisturbed medium (constant)
C_d	drag coefficient
C_l	lift coefficient
$C_{l\alpha}$	2D lift curve slope of the airfoil section comprising the rotor
C_T	thrust coefficient
D	rotor diameter
D_v	vehicle diameter
dF	blade loads
dS	differential surface area
F	Prandtl's tip loss function
f	implicit function defining data surface ($f = 0$)
$H(f)$	Heaviside step function
$\vec{l}$	loading vector acting on fluid
M	Mach number
$\hat{n}$	outward unit normal vector
N_b	number of blades
ΔP_{ij}	perturbation compressive stress tensor
p	pressure
p'	acoustic pressure
Q	torque
R	blade radius
r	distance between noise source and observer, $\lvert\vec{x} - \vec{y}\rvert$
t	observer time
$\vec{u}$	fluid velocity
u_n	local normal velocity of fluid
$\vec{v}$	surface velocity
v_n	local normal velocity of source surface
$\vec{x}$	observer position
$\vec{y}$	noise source position

Greek Letters

α	angle of attack
$\delta(f)$	Dirac delta
δ_{ij}	Kronecker delta
θ	pitch angle / elevation angle
λ	inflow ratio
σ	solidity
τ	source time
φ	inflow angle
ψ	azimuth angle
Ω	rotation rate

Abbreviations

AAM	Advanced Air Mobility (In this thesis AAM is effectively synonymous with UAM, but not restricted to urban environments)
APTH	Acoustic Pressure Time History
BEMT	Blade Element Momentum Theory
BET	Blade Element Theory
BPM	Brooks, Pope, Marcolini
BVI	Blade-Vortex Interaction
BWI	Blade-Wake Interaction
CAA	Computational Aeroacoustics
CHARM	Comprehensive Hierachial Aeromechanics Rotorcraft Model
CFD	Computational Fluid Dynamics
eVTOL	Electric Vertical Take-Off and Landing
FW-H	Ffowcs Williams-Hawkings
HSI	High Speed Impulsive
LBL-VS	Laminar Boundary Layer Vortex Shedding
OASPL	Overall Sound Pressure Level
OpenVSP	Open Vehicle Sketch Pad
ret	Evaluated at the Retarded Time
SPL	Sound Pressure Level
sUAS	small Uncrewed Aerial Vehicle
TBL-TE	Turbulent Boundary Layer-Trailing Edge
UAM	Urban Air Mobility
UAS	Uncrewed Aerial Vehicle

Acknowledgments

There are so many people that I am grateful for. Firstly, I would like to thank Dr. Brentner for his help and for allowing me to participate in FAA ASCENT Project 77. Despite my slow progress, he kept giving me useful advice to advance my research skills. Dr. Greenwood also supported me despite his busy schedule. I really should mention my lab mates because of their help: Ted Gan, Bhaskar Mukherjee, and Rob Rau. I cannot describe my gratitude here. Without their help, I would not be able to finish my work. I would like to thank Dan Weitsman for providing me with VSP2WOPWOP and helping to debug the issues. It is unimaginable how I would have been able to do the work without his help. I am also grateful to Demi Zachos for her work on the generic eVTOL studies, which I have no doubt helped to clarify the work on the far field distance for multicopter. Lastly, I am grateful for my family in Korea who supported and believed in me all my entire life. Without their help, I would not be able to study or do the research.

This research was funded by the U.S. Federal Aviation Administration (FAA) Office of Environment and Energy (AEE) through ASCENT, the FAA Center of Excellence for Alternative Jet Fuels and the Environment, Project 77 through FAA Award Number 13-C-AJFE-PSU Amendment No. 76 managed by Dr. Hua (Bill) He of AEE. Any opinions, findings, conclusions, or recommendations expressed in this material are those of the authors and do not necessarily reflect the views of the FAA.

Dedication

I dedicate this thesis to my family, who supported me my entire life.

Chapter 1 Introduction

1.1 Overview

Urban Air Mobility (UAM), which is defined as safe and efficient air traffic operations in a urban area for both manned aircraft and uncrewed aircraft systems, is the focus of research and development by industry, academia, and government [1]. Due to its growing popularity, there exist various configurations for UAM, which can be classified into four different types based on its size [2]:

1. Large-scale class UAM are typically associated with the size of commercial regional jets
2. Medium-scale class UAM, the popular concept of UAM, i.e., “air taxi”
3. Small-scale class UAM are the most prevalent in the community space. They are used for aerial photography, civil engineering surveillance, and firefighting.
4. Micro air vehicles, typically with less than 15-cm span [3]. These vehicles are tend to be geared toward implementation of bio-mimicry applications.

Figure 1.1. Examples of various size UAMs [2].

In the future, the operation of these vehicles is expected to increase. As shown in Fig 1.2, by 2050, the UAM market may generate revenues of approximately 90 billion USD per year [4]. However, it is highly likely that UAM could face certain challenges as its popularity increases.

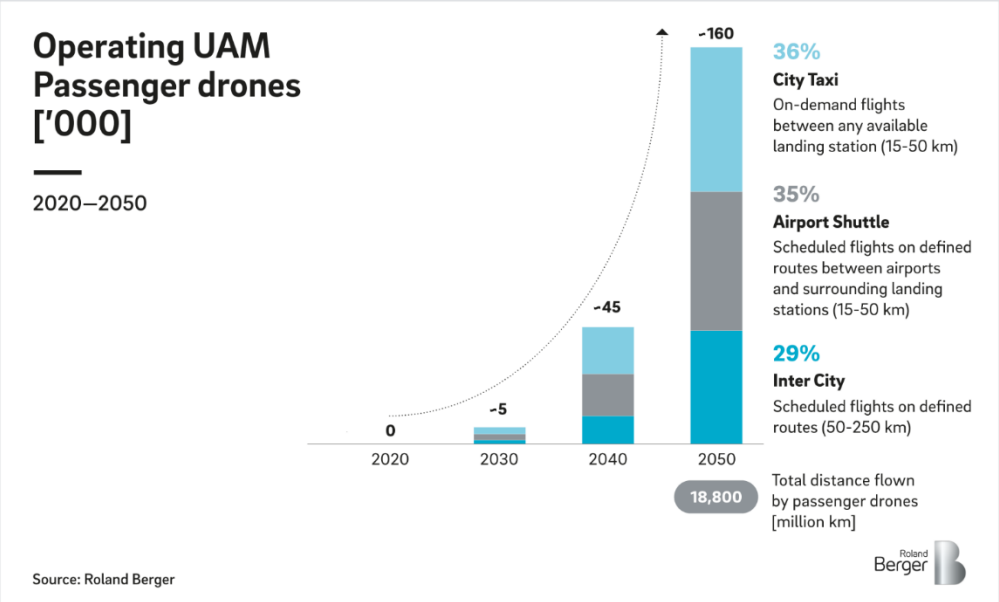

Figure 1.2. Prediction of the value of UAM market [4].

Therefore, specific aspects should be addressed to ensure public acceptance: safety, privacy, impact on job markets, impact on environment, visual disruption and noise [5].

Safety: Safety should be assured if UAM is to be incorporated into the transportation system [6]. Two major accident scenarios are expected, based on a prognostic survey on accident investigation experts: Ground pilot human error or omission and autonomous control system failure. These scenarios should be considered during the conceptual design process. Also, data recorders should be used to investigate accidents. This suggests that installation of recoders on UAM should be considered a mandatory design requirement [6].

Privacy: Privacy breaches can occur during UAM operations. For example, unsuspected

collection of information during the flight can cause privacy violations [7]. Also, it was found that bystanders (i.e., people who had no experience operating drones but may be surrounded by flying drones) had various privacy concerns about drones such as stalking, photo/video recording, and sharing [8], [9]. Cavouskian [10] suggested comprehensive principles of UAM privacy, which is to reroute the flight path of UAMs. Smart routing technology can allow UAMs to routinely avoid areas that are specified as private. For instance, DJI, a drone manufacturing company, incorporated a static approach for restricted area recognition in which property coordinates are compiled into the vehicle software. However, some issues must be addressed before this system is adopted such as property restrictions that are compiled into the vehicle software and the capability of accounting for the specific situations.

Job Market impact: The job market is likely to be considerably impacted by UAM. For example, many e-commerce firms such as Amazon, Google, and WalMart are launching delivery services via drones [11], [12], which can affect the labor market. Reduction in the employment of delivery drivers is expected when the use of drones in the logistics sector becomes widespread [13].

Another job sector that can be impacted in many ways by sUAS is the construction industry [14]. For one specific example, drones can serve as surveyors or inspectors. The productivity of a drone can exceed that of a person because inspections can be more efficient in terms of speed and safety. Issues such as the above should be addressed before incorporating AAM into society.

However, some studies suggest the possibility of coexistence between humans and AAM. Crisan and Nechita [15] conducted a study on a truck and drone delivery system that can cooperate with each other. Crisan and Nechita introduced a heuristic for minimizing the total transportation time of a truck-and-drone delivery system.

Environmental impact: Various environmental concerns are expected to emerge as the popularity of UAM increases [14]. For example, just as birds collide with wind turbines, they

can collide with flying drones. In this process, debris from lost or abandoned goods can cause issues. In addition, energy consumption may increase with the operation of AAM.

Conversely, UAM could be employed as a tool to improve the environment. Obaid et al. [16] suggested that drones can be used to detect waste and inform people to dispose of it. Thus, this technology can be used to promote individual and societal behavioral changes. Also, AAM can be used to promote sustainable agriculture [17]; unused fertilizers pollute the environment by generating greenhouse gases, but drones can locate them using various sensors. Finally, drones can be used to reduce air pollution; they can destroy pollutants by spraying water and chemicals into the atmosphere [18]. Further research on the potential of AAM with regards to its use in improving the environment is needed.

Visual disruption: Complaints could arise against the presence of UAM in the sky. Given the similarities in the concerns arising in UAM and wind turbines, the visual effect is examined for the case of wind turbines. Devlin [19] suggested that visual disruption is the largest impact caused by the presence of wind turbines. It should be noted that visual impact has positive as well as negative impact [20]. Specifically, the view is dependent on the type of the landscape. Hence, there is a possibility that UAM would likely be accepted by people in some regions.

As the annoyance toward wind turbines is caused by the spatial difference between costs and benefits (this principle would also apply in other topics such as the noise), by allowing those who are most affected to benefit from turbines, the annoyance could likely be reduced. Likewise, considering the balance between these two factors would be helpful in avoiding the disapproval of people affected by UAM.

Noise: This thesis focuses specifically on noise as it is related to other topics such as environment and visual disruption. For instance, it is expected that the noise of UAM can cause distress to animals (including humans) [21]. Fortunately, the effect of drone noise was found to be minimal on submerged animals [22] and birds [23]. However, more studies should be conducted to be

assured that the noise of UAM would not have a detrimental effect on other animals. Also, it is known that visible noise sources are linked to increased annoyance [24].

To mitigate the noise, low-noise design by considering factors such as rotor tip speed, airfoil shape, and rotor orientation [25] or noise abatement procedures [26] are needed [27]. As shown in Figure 1.3, noise reduction technologies have been integrated into commercial aircraft design to reduce aircraft noise levels gradually over the years [28]. The stages referred in Figure 1.3 are regulatory levels enforced by civil aviation authorities, which were made more stringent as technology to reduce the noise was improved. Similarly, regulations for the noise generation of helicopters are well established. But given the low rotor tip speeds and complex flight operations of UAM, it is difficult to incorporate helicopter noise abatement techniques to UAM scenarios. [29]. Specifically, it is known that reducing the tip speed decreases the tonal noise [27], and with many rotors, propellers, and fixed aerodynamics surfaces, unsteady aerodynamic interactions between these components are expected [29]. Another challenge to the analysis of UAM noise is that since the characteristics of UAM noise are expected to be different from that of conventional aircraft or helicopters, it is expected that new noise exposure and annoyance from UAM could hinder their integration into the transportation system [28]. For example, it is known that drone noise is substantially more annoying than road traffic or aircraft noise due to special acoustic characteristics [24]. Also, it is known that one aircraft design might have a different acoustic field from another design with regard to its spectral and temporal characteristics [28], which implies that current metrics may not be as effective for other cases even if those metrics are appropriate for some instances [30]. Therefore, further research should use computational or experimental methods for better understanding of UAM noise.

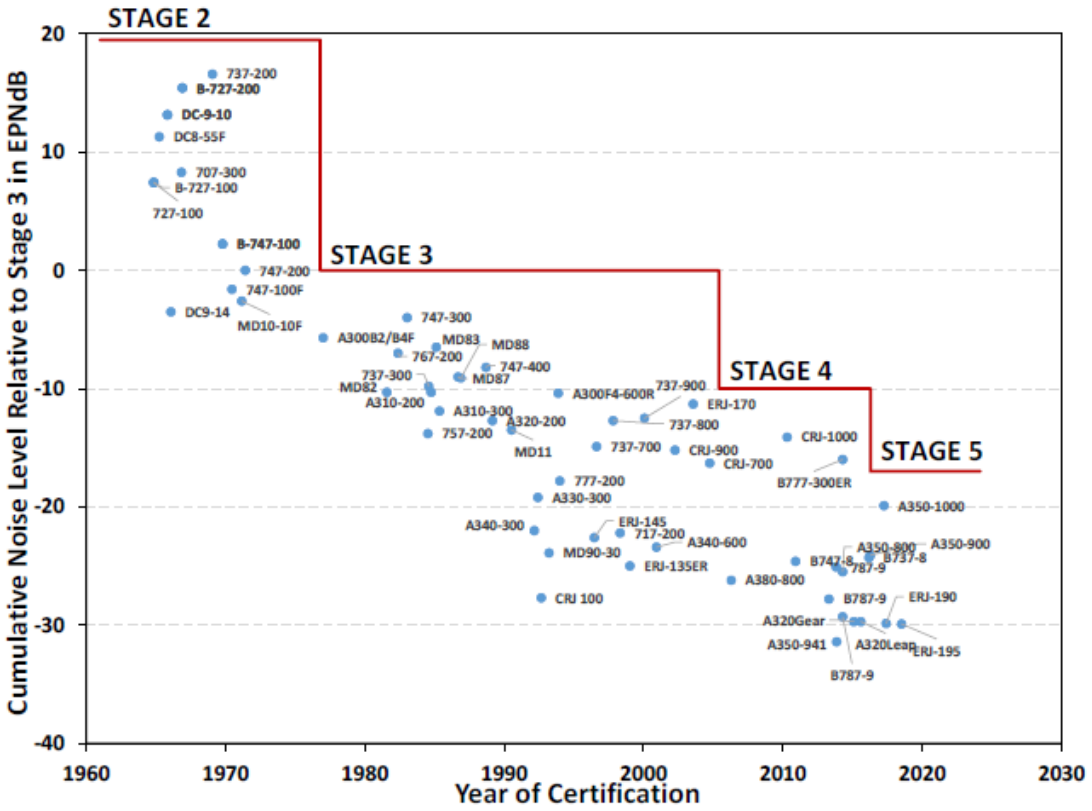

Figure 1.3. Commercial transport noise cumulative noise level reduction relative to Stage 3 **[28]**.

1.2 Far-field Distance

Accurate measurement of the noise is crucial for understanding noise generation. To accomplish this goal, this thesis identifies the appropriate far-field distance for UAM so that measurements are made in a region where acoustic pressure waves, instead of evanescent pressure waves, dominate the signal [31].

There are many definitions for far-field distance. However, among those definitions, there is a common principle that SPL decreases by 6 dB for a doubling of the distance in the far-field [32]. As shown in Figure 1.4, SPL is not decreasing linearly in the near field. This implies the difficulty of predicting the noise in this region and the necessity of assuring that microphones are placed in the far field.

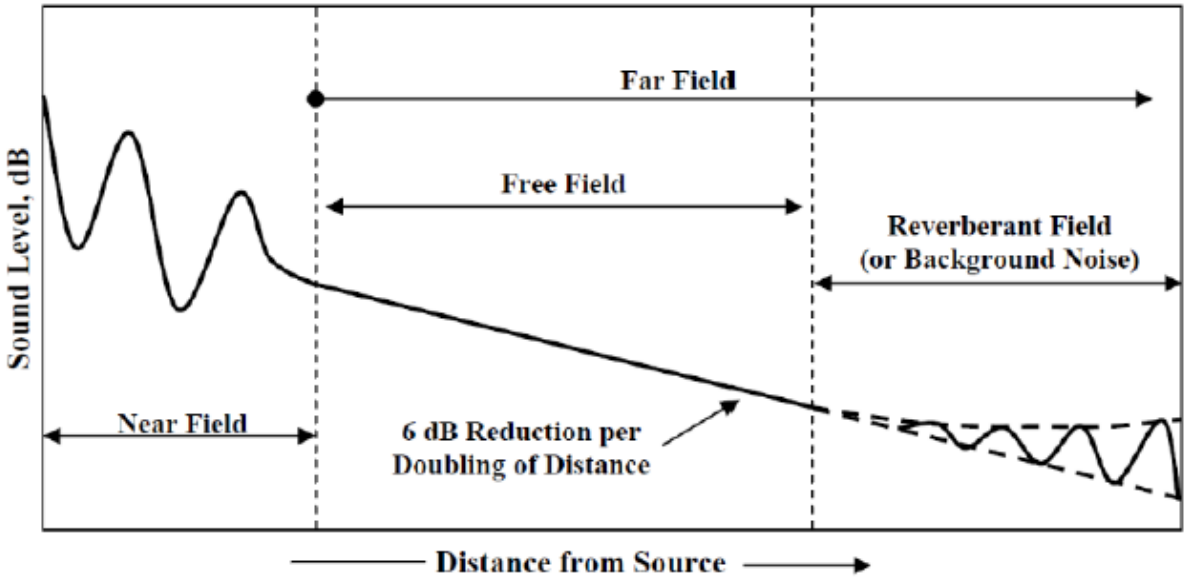

Figure 1.4. Definitions of the sound field [32].

It is known that the beginning of the acoustic far field for helicopter rotors is approximately 5 rotor diameters away from the hub, but similar guidance for UAM have not been established. Regarding the far-field distance studies on UAS, Turkdogru and Ahuja [33] found that 10 rotor diameters and 25 rotor diameters for unducted and ducted rotors, respectively, were in the acoustic far field. On the other hand, Tinney and Sirohi [31] found the far-field distance to be 4.1 or 3.3 rotor diameters for rotors with a diameter of 9 in and 12 in, respectively. Finally, Van Treuren et al. [34]. conducted research on the far-field distance by using the hemispherical grid which includes the out-of-plane, and found that SPL does not follow 1/r law until the distance from the source and the vehicle reaches 28 diameters in most directions. To summarize, there are some discrepancies among these results and this implies that research should be conducted to set up a consistent rule of thumb for the far-field distance of UAM. Therefore, this thesis examines the far-field of the UAM with various conditions to set up a rule of thumb for the far-field distance regarding the UAM.

1.3 Thesis Objective

The thesis's objective is to develop a computational method to set up a rule of thumb for the far-field distance of UAM so that measured or predicted noise can be generalized from one far-field distance to any other [35]. The coupled system of OpenVSP [36], [37], VSP2WOPWOP [38] (or CHARM [39]–[42]), and PSU-WOPWOP [43], [44] is used for this purpose. Specifically, OpenVSP is used for generating the computational geometry of aircraft components (see Section 3.1). In addition, both VSP2WOPWOP and CHARM are employed to compute the air loads using blade element momentum theory (BEMT) [45] and constant vorticity contour -free wake method [35], [41], respectively (see Sections 3.2 and 3.3). Finally, noise prediction is done by using PSU-WOPWOP, with Ffowcs Williams-Hawkings (FW-H) equation for the tonal noise and Brooks, Pope, and Marcolini (BPM) model for the broadband noise predictions (see Section 3.4). With this noise prediction system, the author has conducted parametric studies (i.e., number of rotors, size of the vehicle, and flight states) to examine the parameter's influence on the far-field distance and the directivity of the far-field distance.

1.4 Contributions

The effect of a number of rotors and vehicle size on the far-field distance regarding the case of hovering sUAS was examined to cover various conditions and situations. Proportionality between both the number of rotors and vehicle size and the far-field distance was found when the distance was normalized by the diameter of the rotor. Also, when the distance was normalized to the diameter of the vehicle (a diameter circumscribing the vehicle) it was found that the results are ranging from 1.5 D_v to 2.0 D_v for cases with multiple rotors. This indicates that the normalization by the vehicle diameter may be more appropriate than that of the rotor diameter.

Also, the far-field distance study was conducted for the case of a generic eVTOL, which has a

larger size and different operating conditions compared to the sUAS. Both hovering and forward flight conditions were considered. It was found that the far-field distance was approximately 5.6 D_v (both hover and forward flight cases, assuming the noise source is a full vehicle), which is approximately 3.3 times compared to the case of sUAS. This implies that the flight state does not significantly affect the far field distance although different rules for the far-field distance among different configurations of UAM are may be required.

1.5 Reader's Guide

- Chapter 2 explains the theory of rotorcraft aeroacoustics and points out the difference between conventional helicopters and UAM.
- Chapter 3 describes the noise prediction system of OpenVSP, VSP2WOPWOP or CHARM [39]–[42], and PSU-WOPWOP.
- Chapter 4 provides the interpretation of the results on far-field distance and describes the interrelationship between both numbers of rotors, vehicle size, and far-field distance, for the case of hovering sUAS. Also, for the case of generic eVTOL, both hovering and forward flight cases are employed and examine its effect on the far-field distance. Comparisons between results for sUAS and a generic eVTOL are made.
- Chapter 5 concludes the thesis by summarizing the results and providing directions for future research.

Chapter 2

Aeroacoustic Theory

The discipline of aeroacoustics was developed by Sir James Lighthill when he introduced the acoustic analogy [46], [47]. Ffowcs Williams and Hawkings [48] generalized the acoustic analogy by employing generalized function theory to consider the effects of general types of surfaces and motions. By using a Green's function approach, Farassat introduced many integral formulations [49], among which the most widely used is Farassat's formulation 1A [50].

Noise sources can be classified as deterministic and nondeterministic, as shown in Figure 2.1 [29]. Deterministic noise is a combination of some or all of the following noise sources: thickness, lower harmonic loading, blade–vortex interaction (BVI), and rotor–airframe interaction. Nondeterministic noise is due to broadband noise sources, such as: blade–wake interaction (BWI), blade self-noise, atmospheric turbulence ingestion, and turbulent wake ingestion. Noise sources due to unsteady loading are highlighted in blue in Figure 2.1.

Details and how these noise sources differ between conventional helicopters and UASs will be explained in the following sections. Previous studies [29], [51] have examined these topics in detail.

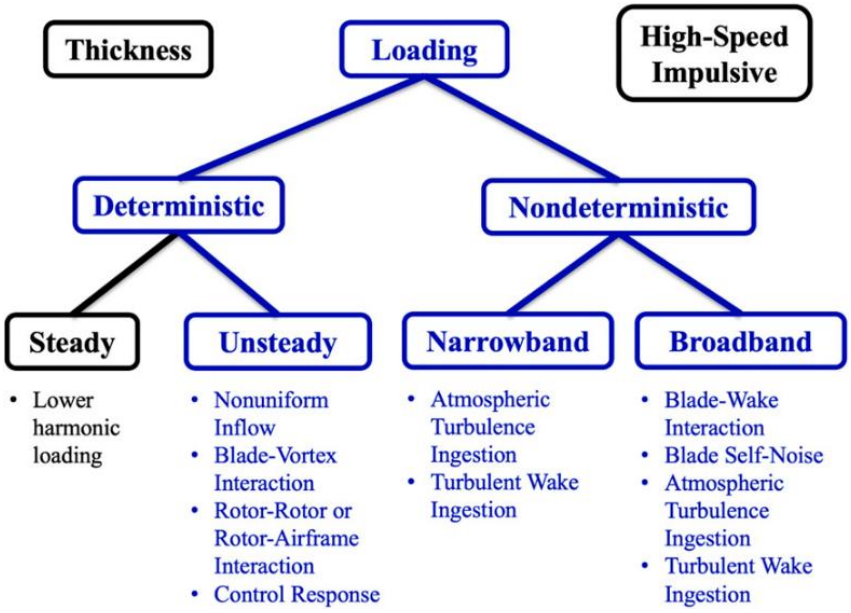

Figure 2.1. Taxonomy of rotor noise sources [29].

2.1 Ffowcs Williams and Hawkings Equation

The Ffowcs Williams and Hawkings (FW-H) equation [48] is an exact rearrangement of the continuity equation and Navier–Stokes equations into the form of an inhomogeneous wave equation with two surface source terms and one volume source term, i.e., monopole, dipole, and quadrupole, respectively [49]. The FW-H equation may be written as follows:

$$\Box^2 p'(\vec{x},t) = \frac{\partial}{\partial t}[\{\rho_0 v_n + \rho(u_n - v_n)\}\delta(f)] - \frac{\partial}{\partial x_i}[\{\Delta P_{ij}\hat{n_j} + \rho u_i(u_n - v_n)\}\delta(f)] + \frac{\partial^2}{\partial x_i \partial x_j}[\{\rho u_i u_j + P_{ij} - c^2\rho'\}H(f)] \quad (2.1)$$

where

$$\Box^2 = \frac{1}{c^2}\frac{\partial^2}{\partial t^2} - \nabla^2 \quad (2.2)$$

This is the most general form of the Lighthill acoustic analogy and can be used for predicting the noise generated by the motion of rotors, propellers, and maneuvering aircraft [27]. When a moving surface, such as a rotor blade, is chosen for the data surface (i.e., impermeable data surface); $f = 0$, the no-penetration condition of $u_n = v_n$ is satisfied and the wave equation is simplified. In this situation, discontinuities between the interior and exterior of the data surface

occur, but this is addressed using a generalized function theory, which can deal with the differentiation of discontinuous functions [49].

The monopole term (first term on the right side of Eqn 2.1) can be regarded as thickness noise when the data surface is impermeable, while the dipole term (second term on the right side Eqn 2.1) is known as the loading term [27]. Thickness noise is due to the displacement of the fluid in the flow field by the rotor blade, whereas loading noise is caused by the accelerating force on the fluid generated by the moving blade surface [49]. The Dirac delta function, $\delta(f)$, implies these noise sources are surface sources. In contrast, in Eqn. 2.1, the quadrupole term acts only outside of the data surface. In other words, quadrupole term is a volume source term [29], and this is indicated by the Heaviside function, $H(f)$ [49]. This term can be used to correct the propagation of the monopole and dipole sources to account for deviations from the linear wave equation [29]. One example of when the quadrupole source is needed would be high-speed-impulsive (HSI) noise, which occurs at transonic or supersonic tip speeds. As it is expected that UAM vehicles operates at a low tip Mach numbers, the quadrupole term can be neglected. Furthermore, for conventional aircraft, the quadrupole source has often been neglected in noise prediction owing to the computational demands of determining the flow field with sufficient accuracy to be used for noise prediction and the computational challenge of volume integration in the acoustic prediction [49].

By placing a fictitious surface in the flow off the body, the effect of quadrupole noise sources within that surface is contained in the surface source terms of the FW-H equation. When the FW-H equation is used in this manner, it is called the permeable surface formulation [49]. By using this method, without integrating the entire volume, phenomena such as acoustic shadowing and reflection off the vehicle as well as near-field nonlinear propagation, which are usually predicted in computational aeroacoustics (CAA) based on CFD, can be predicted [29], [49]. However, the outer volume still needs to be integrated to account for the flow features outside the surface, such as vortices, and to remove spurious signals [52]. Despite this disadvantage, if

the permeable surface is chosen appropriately, it can generate good results that are not significantly affected by spurious noise [53].

2.2 Farassat Formulation 1A

By employing the free-space Green's function, Farassat's Formulation 1A can be obtained [49], and when the quadrupole term is neglected, Formulation 1A can be written as follows [29]:

$$p'(\vec{x},t) = p'_T(\vec{x},t) + p'_L(\vec{x},t) \quad (2.3)$$

$$4\pi p'_T(\vec{x},t) = \int_{f=0}\left[\frac{\rho_0(\dot{v}_n+\dot{v_n})}{r(1-M_r)^2}\right]_{ret}dS + \int_{f=0}\left[\frac{\rho_0 v_n\left(r\dot{M}_r+c_0(M_r-M^2)\right)}{r^2(1-M_r)^3}\right]_{ret}dS \quad (2.4)$$

$$4\pi p'_L(\vec{x},t) = \frac{1}{c_0}\int_{f=0}\left[\frac{\dot{L}_r}{r(1-M_r)^2}\right]_{ret}dS + \int_{f=0}\left[\frac{L_r-L_M}{r^2(1-M_r)^2}\right]_{ret}dS + \frac{1}{c_0}\int_{f=0}\left[\frac{L_r(r\dot{M}_r+c_0(M_r-M^2))}{r(1-M_r)^3}\right]_{ret}dS \quad (2.5)$$

Three important aspects of Eqns 2.4 and 2.5 are the Doppler factor, retarded time, and the near-field and far-field terms.

The Doppler factor $1/|1-M_r|$ [25], increases as the source approaches to the observer [29]. Similarly, as the source retreats away from the observer the noise is reduced. It should be noted that not only the direction but also the speed and blade motion affect the Doppler factor, and therefore, the noise [29].

The subscript ret in the integrals represents the retarded time, and implies that the integrand is computed when the sound was emitted, i.e., at the time and location of the source such that the sound reaches the observer position at the observer time [25]. Eqn 2.6 and Figure 2.2 can be used to explain this concept [25]. Specifically, when the observer time is known (i.e., *t*), the retarded time (i.e., τ) can be calculated by employing Eqn 2.6.

$$\tau = t - \frac{r}{c_0} \quad (2.6)$$

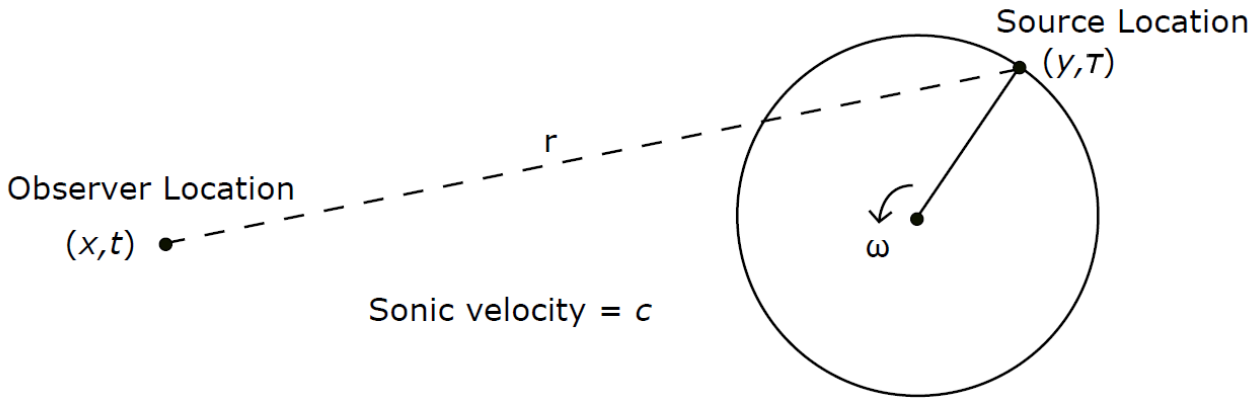

Figure 2.2. Ideas of retarded time and advanced time [25], [45].

Finally, as the noise decay follows the 1/r law, the terms that depend on $1/\mathrm{r}$ are regarded as far-field terms while the terms depending on $1/r^2$ are the near-field terms [29]. When the distance between the source and observer is larger or equal to far-field distance, the terms with 1/r become dominant.

Despite its complicated form, Formulation 1A has the advantage that numerical differentiation of integrals is not required [49].

2.3 Unsteady Noise Sources

It is expected that unsteady noise sources will become dominant for eVTOL aircraft [29]. This is because tonal noise decreases when the tip Mach number is reduced [27]. This should be more noticeable for UAM rotors operating at a low-tip Mach number. As shown in Figure 2.1, unsteady noise source can be divided into deterministic and nondeterministic noise: Deterministic loading noise sources are comprised of nonuniform inflow, blade-vortex interaction (BVI) interaction, rotor–rotor or rotor–airframe interaction, and control response. Nondeterministic noise sources consists of blade-wake interaction (BWI), blade self-noise, atmospheric turbulence ingestion, and turbulent wake ingestion noise (as organized in Figure 2.1) [29]. Understanding these noise sources is crucial for finding the appropriate tip Mach

number so that both tonal and broadband noise can be mitigated [29], [54]. Brief descriptions of unsteady noise sources are given below [29]:

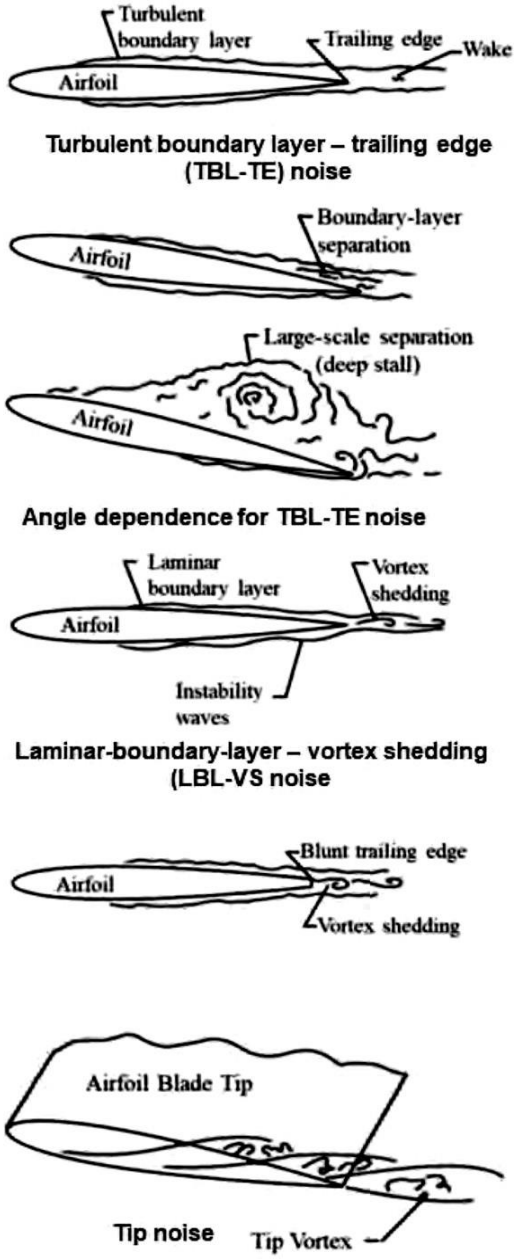

Figure 2.3. Airfoil self-noise sources modeled by Brooks, Pope and Marcolini [55].

Blade-vortex interaction noise: Blade-vortex interaction (BVI) occurs during descent and is generated by the interaction between the rotor and its own wake. Impulsive radiation occurs owing to rapid fluctuations in the aerodynamic loads. These aerodynamic fluctuations are

strongly dependent on the relative positions of the blades and wake (especially the tip vortex), implying that it can be reduced by adjusting the operating condition [56].

Rotor–rotor interaction noise: There exists many situations for rotor-rotor interaction noise. For example, when axial separation between counter-rotating rotors is increased, the broadband noise would likely become the dominant noise source [57] owing to the breakdown of the rotor wake into nondeterministic structures at long wake ages. Also, Lakshminarayan and Baeder [58] conducted a computational study on a pair of counterrotating coaxial rotors and found impulsive loading on both rotors. Moreover, various factors such as blade planform or operating condition can affect the rotor-rotor interaction.

Rotor–airframe interaction noise: Noise can be affected by interaction between rotor and airframe. It is known that the rotor is affected by the airframe and vice versa [59], [60]. Furthermore, re-radiation should be considered especially for the UAM compared to conventional aircrafts. An important example of this is when the propeller wake interacts with a downstream wing, which then can generate (or re-radiate) significant noise.

Blade–wake interaction noise: Blade-Wake-Interaction (BWI) noise is the interaction between rotor blades and their own shed turbulent wakes or the turbulent wake of one rotor interacting with another [27], [61]. It is known that although BWI noise is broadband noise, BWI noise frequency content is between the deterministic noise sources and self-noise sources. Although the exact causes of BWI noise is complicated, two prediction methods exist, described in Brooks and Burley [51] and Glegg et al. [62]. Further improvement in prediction is needed by characterizing rotor wakes at long wake ages.

Airfoil self-noise: Blade self noise originates from many sources, such as shown in Fig 2.3: turbulent boundary layer – trailing edge (TBL-TE) noise, separation and stall noise, trailing edge bluntness – vortex shedding noise, laminar boundary layer – vortex shedding (LBL-VS) noise, and tip vortex formation noise. The noise prediction model developed by Brooks, Pope, and

Marcolini (BPM) [55] is usually employed for UAM, and it is a semi-empirical model that uses the boundary layer characteristics for the NACA 0012 airfoil. This model neglects spanwise flow and the time-dependent effects of unsteady aerodynamics, which can affect the accuracy of noise prediction.

Ingestion noise: This noise occurs when the rotor ingests turbulence and consists of leading edge, atmospheric turbulence ingestion, and wake ingestion noise.

Chapter 3

Noise Prediction System

In this chapter, the noise prediction system is explained. First, Open Vehicle Sketch Pad (OpenVSP) [36], [37] was used to generate the computational geometry of aircraft components [36] needed for aerodynamic analysis [38]. Next, VSP2WOPWOP [38] was employed to compute airloads. Aerodynamic coefficients were extracted from XFOIL [63]. Also, a mid-fidelity aerodynamic tool was used for the computation of blade loads for the case of a generic eVTOL. Specifically, the Comprehensive Hierachial Aeromechanics Rotorcraft Model (CHARM) rotorcraft analysis code [39]–[42] using a novel constant vorticity contour-free wake method [35], [41] (developed by Continuum Dynamics, Inc.) was used for airloads predictions. CHARM computes the aerodynamic interaction between rotors, so rotor-rotor and rotor-wake interactions can be considered.[1] Finally, PSU-WOPWOP [43], [44] was used for noise prediction, with the FW-H equation used for tonal noise prediction and the BPM model for airfoil self-noise. A schematic that explains how noise prediction is organized is shown in Figure 3.1.

[1] Damaris Zachos' performed all the computations for the approximate S-76 and generic eVTOL models using CHARM. Zachos work was part of a joint paper [35], so it is included in this thesis for completeness.

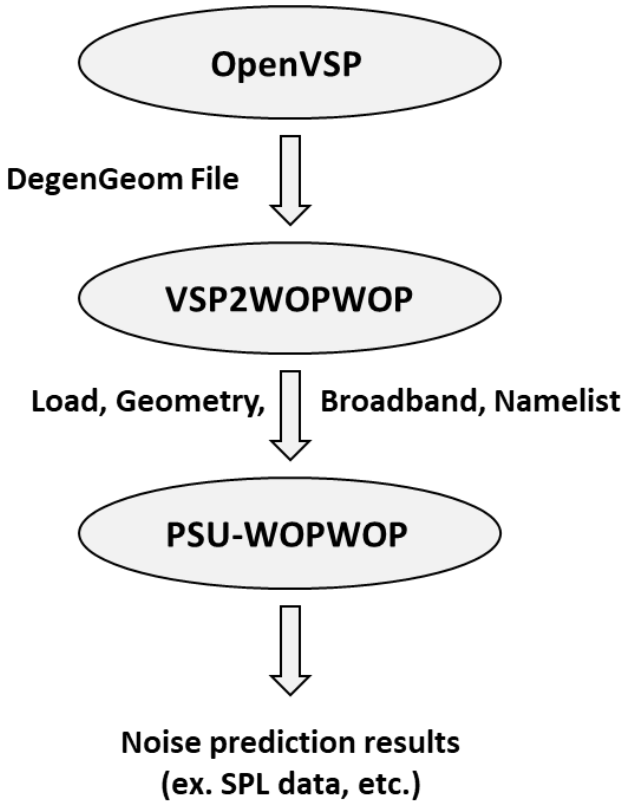

Figure 3.1. Noise prediction system.

3.1 OpenVSP

Open Vehicle Sketch Pad (OpenVSP) is a geometry modeling program that is specifically designed for use in the aircraft conceptual design phase [36], [37]. It is utilized for several engineering analyses and output files that can be used by many other analysis tools [64]. This program also offers parametric variations, which can help capture the intent of the designer. Owing to these benefits, it is adopted by industry, government, and academia as well as startups designing UAVs, eVTOL, civil supersonics, hypersonics, space launches, and small satellites.

As shown in Figs 3.2 and 3.3, which are snapshots from OpenVSP, the computational model of a propeller can be created by manipulating the continuous function of properties (chord, twist, rake, skew, sweep, axial offset, tangential offset, thickness, and design lift coefficient), which are defined as a function of the radius [65]. Among these properties, the distributions of chord, twist, and thickness were considered while implementing the computational blade model of the

Tarot X8. The Tarot X8 octocopter shown in Figure 3.4 was employed by Penn State [66] for flight tests at the Mid-State Regional Airport in Philipsburg, PA. Only the rotors were used in the computational model of the Tarot X8 vehicle.

3.1.1 Generation of Computational Geometries

Two different blade sets, which are called “plastic” and “carbon” (Penn State [66] conducted a flight test using these two blades), were used during flight testing and were approximated in the computational modeling. Although the name of the blade suggests its material, the roughness of the blade was not considered in the aerodynamic analysis or noise prediction. Instead, a tripped boundary layer was assumed for both cases, which is explained in Section 3.3.2 in detail. Also, parameters such as chord, twist, thickness, and diameter were taken into account. A brief overview of the parameters is presented in Table 3.1.

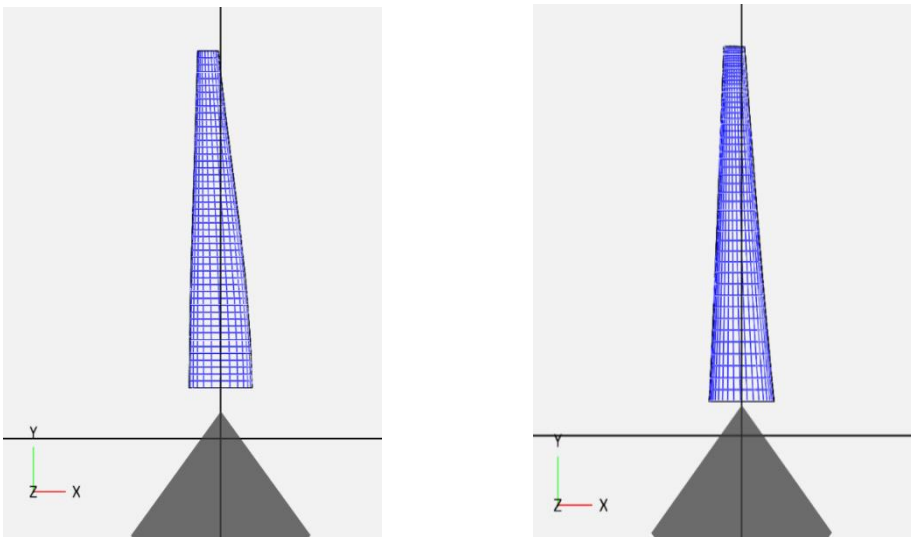

(a) Plastic blade. (b) Carbon blade.

Figure 3.2. OpenVSP modeled Tarot X8 blades.

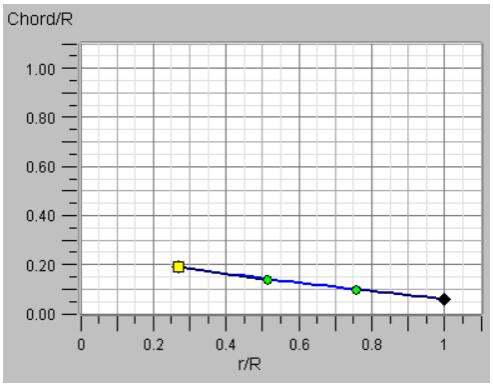

(a) Chord distribution (Plastic).

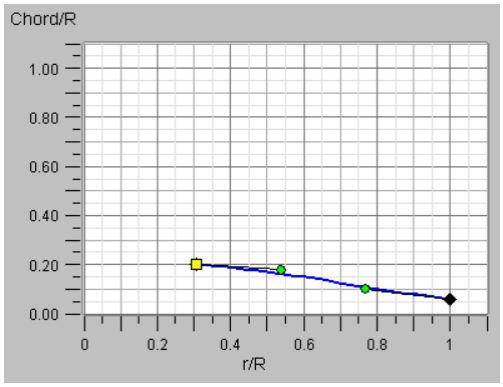

(b) Chord distribution (Carbon).

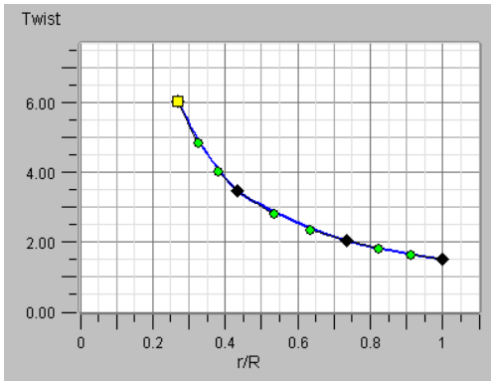

(c) Twist distribution (Plastic).

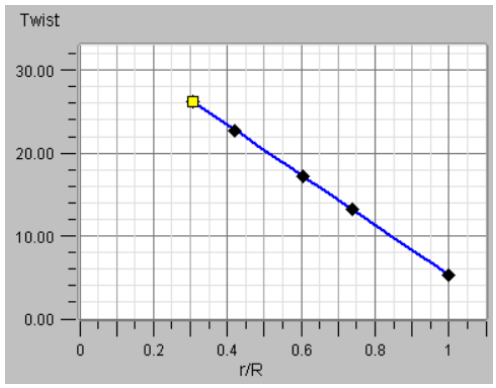

(d) Twist distribution (Carbon).

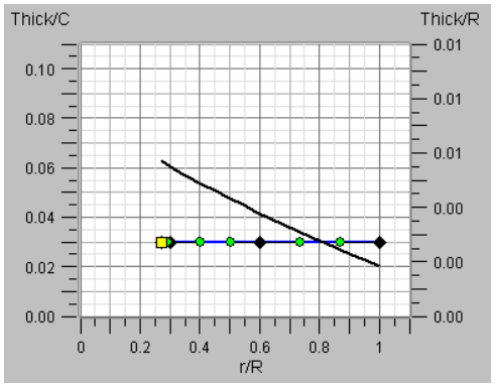

(e) Thickness distribution (Plastic).

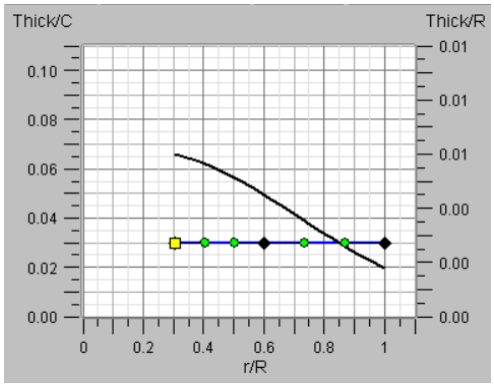

(f) Thickness distribution(Carbon).

Figure 3.3. Chord, twist, and thickness distributions for computational geometries.

Table 3.1 Specifications of plastic and carbon blades.

Parameter	Plastic	Carbon
Diameter (m)	**0.381**	**0.39**
Tip pitch angle (°)	**1.5**	**5.29**
Twist distribution	**Ideal Twist**	**Linear Twist**

Figure 3.4. The real model of Tarot X8 octocopter [66].

Chord was measured at each radial station, which were equally spaced from root to tip. Regarding the twist distribution, the assumption was made that the plastic blade has ideal twist based upon its shape. A pitch gauge was employed for the case of carbon blade to measure the pitch angle. The thickness distribution values were assumed to be very thin by referring to the real model of the blades. The final version of computational geometries for both plastic and carbon blades is shown in Figure 3.2, while the chord, twist, and thickness distributions are shown in Figure 3.3. As shown in Figure 3.5, the root of the propeller that was not necessary for the aerodynamic analysis was truncated to 0.27 *R*. The plastic design was the primary design used for this research.

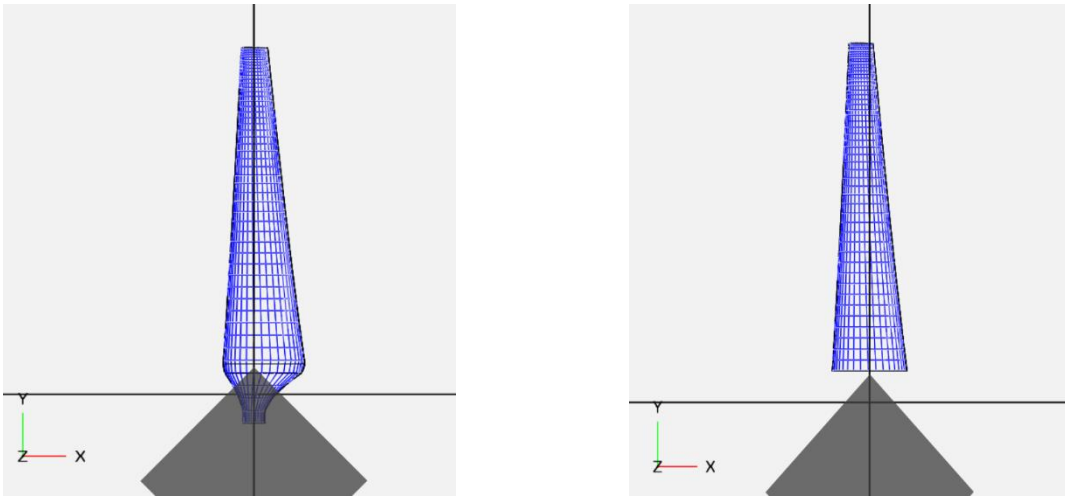

(a) Before manipulation. (b) After manipulation.

Figure 3.5. Plastic blade model, before and after manipulation.

3.1.2 DegenGeom File

When geometries were created, they were converted into a DegenGeom file. The DegenGeom file was developed by Joel Belben with the philosophy that it needed to have 'everything including the kitchen sink' and convey as much information as possible [64]. Specifically, the DegenGeom file contains information in levels of abstraction such as surface, plate, line, and point. The concept is illustrated in Figure 3.6 and can be explained as follows [67]: Degenerate surface (Figure 3.6a) is a suitable level of abstraction for three-dimensional analysis methods, such as an aerodynamic panel method or acoustic scattering code. Also, the degenerate plate (Figure 3.6b) is suitable for analysis methods that assume the surface is very thin (i.e., Aerodynamic vortex-lattice code, an equivalent-plate structural analysis, or a planar acoustic shielding analysis). The degenerate stick (Figure 3.6c) is suitable for aerodynamic analysis using a lifting-line code, or for structural analysis using an equivalent-beam method. Finally, the degenerate point (Figure 3.6d) is suitable for aerodynamic analysis using empirical or semi-empirical skin-friction analysis.

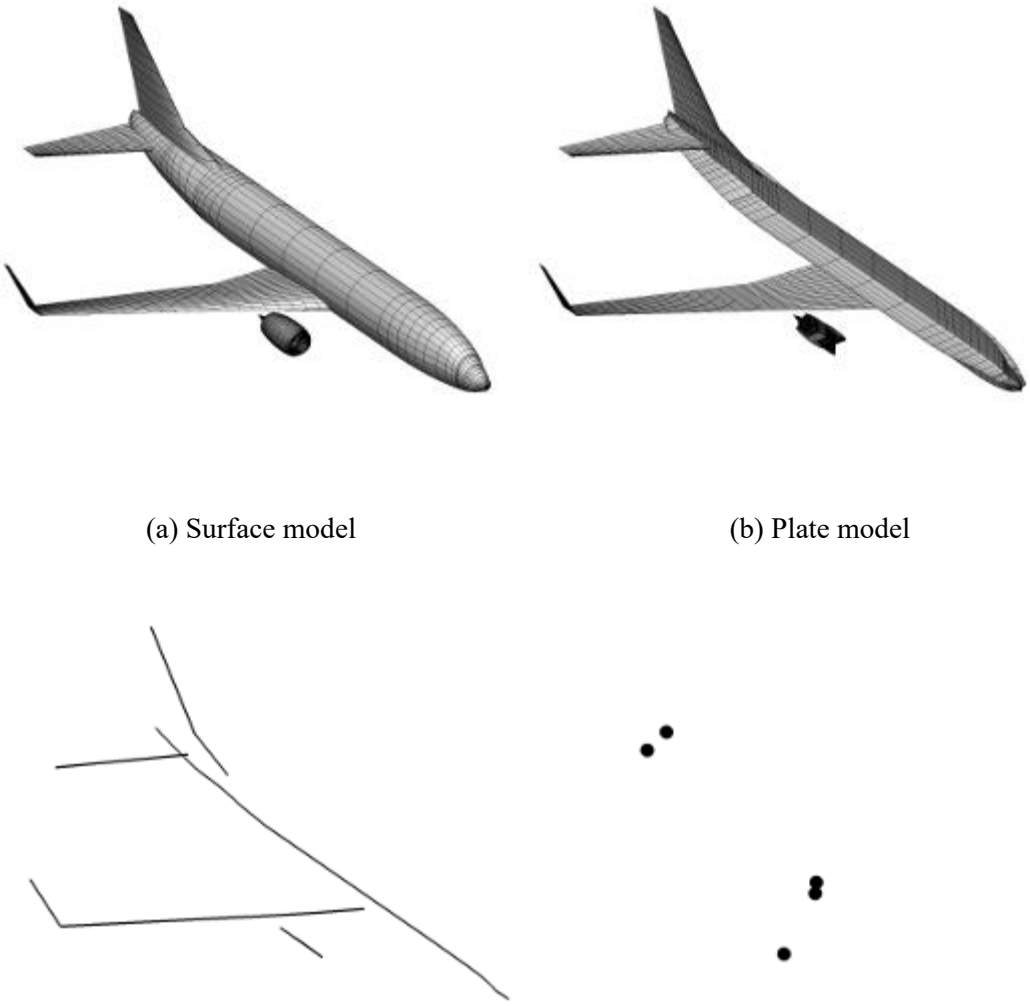

(a) Surface model (b) Plate model

(c) Stick model (d) Point model

Figure 3.6. DegenGeom of a transport aircraft [64], [67].

The DegenGeom file is used as an input file for VSP2WOPWOP. Specifically, the VSP2WOPWOP parses through the DegenGeom file and places the degenerate geometry components in a dictionary, which is then accessible when needed [38]. VSP2WOPWOP is explained in the Section 3.2.

3.2 VSP2WOPWOP

Weitsman et al. [38] developed a computational framework that couples OpenVSP and PSU-WOWOP. Specifically, it uses Blade Element Momentum Theory (BEMT) and Blade Element Theory (BET) to compute the airloads from a DegenGeom file. Three kinds of trim are possible in VSP2WOPWOP: collective pitch trim, cyclic pitch trim, and RPM trim. In this thesis, collective pitch trim was used to meet the target thrust for each rotor. In the code, either the Newton–Raphson method [38] or the Levenberg–Marquardt method [68] can be used, and the former was utilized in this research [69], [70]. When VSP2WOPWOP is executed, operating conditions, compact chord blade loads, and full blade section geometry are generated in VSP2WOPWOP and transferred to PSU-WOPWOP for the noise prediction [38], [69].

The process of calculating the blade loads for the hovering rotor is explained in the following (which follows that described in Leishman [45]). First, Prandtl's tip loss formulation is used for the computation of the inflow distribution, λ. The purpose of using this function is to reduce the thrust in the tip region. The Prandtl's tip loss function, *F,* also known as "circulation loss" due to the reason that it decreases the induced velocity over the tip region and decreases the lift generated there [45], is used for the calculation of the inflow distribution.

Prandtl's tip loss function, *F* can be obtained as follows:

$$f = \frac{N_b}{2}\left(\frac{1-r}{r\varphi}\right) \tag{3.1}$$

$$F = \left(\frac{2}{\pi}\right)\cos^{-1}\exp(-f)) \tag{3.2}$$

Using the tip loss function, inflow ratio, $\boldsymbol{\lambda}$ can be written as follows:

$$\lambda(\mathrm{r}) = \frac{\sigma C_{l\alpha}}{16F}\left(\sqrt{1+\frac{32F}{\sigma C_{l\alpha}}\theta r}-1\right) \tag{3.3}$$

Then, the angle of attack, α, is computed at each radial station as follows:

$$\alpha = \theta - \lambda / r \tag{3.4}$$

Next, aerodynamic coefficients are extracted from XFOIL [63] and utilized for the calculation of thrust and power coefficient:

$$dC_T = \frac{1}{2}\sigma C_l r^2 dr \tag{3.5}$$

$$dC_P = \frac{1}{2}\sigma(\frac{\lambda}{r} C_l + C_d) r^3 dr \tag{3.6}$$

Then, these results are used for the computation of thrust and torque distribution:

$$dT = \rho dC_T(\pi R^2)\ (\Omega R)^2 \tag{3.7}$$

$$dQ = \rho\ dC_P\ (\pi R^2)\ (\Omega R)^2 R \tag{3.8}$$

Finally, thrust and torque distributions are employed for the calculation of blade loads, dF_x, dF_y, dF_z, which are shown in Figure 3.7.

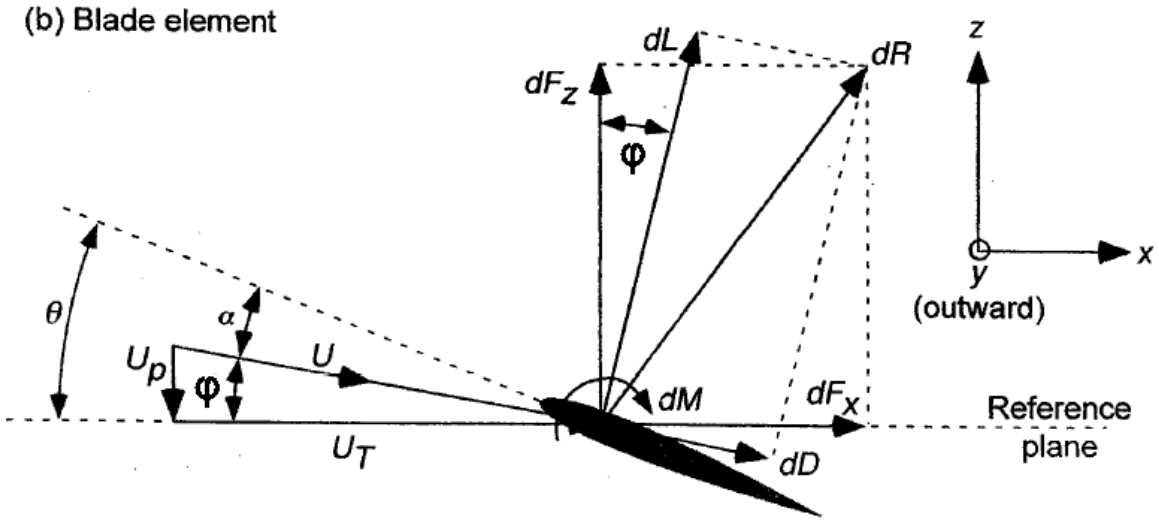

Figure 3.7. Air loads at the element of the blade [45].

Blade loads are obtained as follows:

$$\varphi = \theta - \alpha \tag{3.9}$$

$$dF_x = dL\ \sin\ \varphi + dD \cos\ \varphi \tag{3.10}$$

$$dF_y = 0 \tag{3.11}$$

$$dF_z = dL\ \cos\ \varphi - dD \sin\ \varphi \tag{3.12}$$

Blade loads in the '*y*' direction are ignored following the independence principle [45]. Refer to [45] for more information on BEMT.

3.3 CHARM

Continuum Dynamics Inc.'s CHARM rotorcraft comprehensive analysis code [39]–[42] was utilized to compute the airloads for the generic eVTOL case [71]. CHARM couples a full-span, free-vortex wake model with a vortex lattice, lifting surface, blade aerodynamics model, an elastic blade structural dynamics model that accounts for fully-coupled flap/lag/torsion modes, and a fast doublet panel fuselage model which together provide a capability for modeling complete aircraft aeromechanics for combinations of rotors, props, wing, ducts, tails and airframes [71]. This implies CHARM can conduct higher fidelity aerodynamic prediction, compared to VSP2WOPWOP, and can account for aerodynamic interactions. These features are crucial since the generic eVTOl has different operating conditions compared to sUAS [71].

When coupled with the PSUHelosim flight simulation code, the coupled system provides the necessary information needed for the first principle-based thickness and loading noise prediction and other information required to predict broadband noise [71]. Specifically, PSUHelosim provides trim solution for desired flight trajectory to CHARM in order to calculate the blade loads. Refer to [39]–[42], [71] for more information on CHARM.

3.4 PSU-WOPWOP

3.4.1 Overview

PSU-WOPWOP [72] is a noise prediction tool that employs Farassat formulation 1A for the numerical integration of tonal noise prediction and predicts broadband self noise using either the Pegg model [73] or the BPM model. BPM model was used for this research and detail can be found in Sections 3.3.2 and [37], [55].

It should be noted that PSU-WOPWOP can be used for general-purpose tasks where arbitrary surfaces can be utilized as the geometry [27]. That is, it can be used not only for rotors but also for other parts such as wings [72], [74]. Another important aspect of PSU-WOPWOP is that it employs a source-time algorithm. Although formulation 1A is a retarded-time formulation, there are several approaches to finding the acoustic pressure time history with this formulation [43]. Specifically, the source time, τ, is fixed and the time of arrival to the observer is calculated for points on the blade surface [25]. The algorithm is presented in Figure 3.8 [44]. To accomplish this procedure, information on the source motion and blade loading at the emission time is needed. The data needed by PSU-WOPWOP is computed by VSP2WOPWOP at a sequence of source times and positions, which is the appropriate input to PSU-WOPWOP. During this process, an object called a patch is used, and multiple patches allow users to analyze each section of the blade separately [44]. It should be noted that since the arrival time t will be different for each point, the time history of each point on the surface must be interpolated so that the contributions can be summed at the same observer time t [43]. Refer to [25], [43], [44], [72] for more information on PSU-WOPWOP.

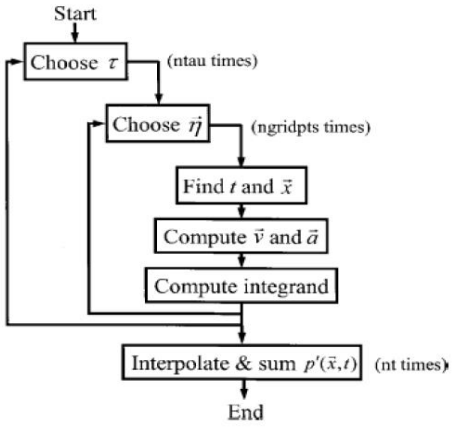

Figure 3.8. Source-time algorithm [44].

Regarding the results of PSU-WOPWOP, usually, acoustic pressure time history (APTH) and spectral contents are analyzed. Specifically, a window function, such as the Hanning window, is applied to APTH followed by a Fourier Transform to obtain the SPL in the frequency domain, and the spectral contents are integrated to generate the overall sound pressure level (OASPL). In this thesis, OASPL is examined to predict the far-field distance.

3.4.2 Validation

Weitsman et al. [38] validated the case of hovering and tonal noise prediction by employing experimental data for a model-scale helicopter rotor. Specifically, data from a 1/5th-scaled Boeing Model 360 that was measured in the DNW wind tunnel [75] was utilized for the validation. For the specifications [38] of the blade, the radius was 1.54 m, a basic chord of 0.13 m, a piecewise linear twist distribution of -9.3°, and a planform taper near the blade tip. VR12 and VR15 airfoil cross sections were used. In addition to this information, the Model 360 rotor is a four-bladed rotor with a thrust-weighted solidity, σ_T = 0.10 and hover tip Mach number, M_H = 0.636 when hovering. Regarding the observers, both in-plane and out-of-plane microphones were employed. The in-plane observer was located 4.6 rotor diameters from the hub and out-of-plane observers were placed 6° above and below the rotor. Although there exists

some discrepancy between the results of experimental and noise prediction, as shown in Figure 3.9, it can be considered negligible. This implies that the noise prediction system of OpenVSP, VSP2WOPWOP, and PSU-WOPWOP can be employed, assuming that appropriate conditions are utilized.

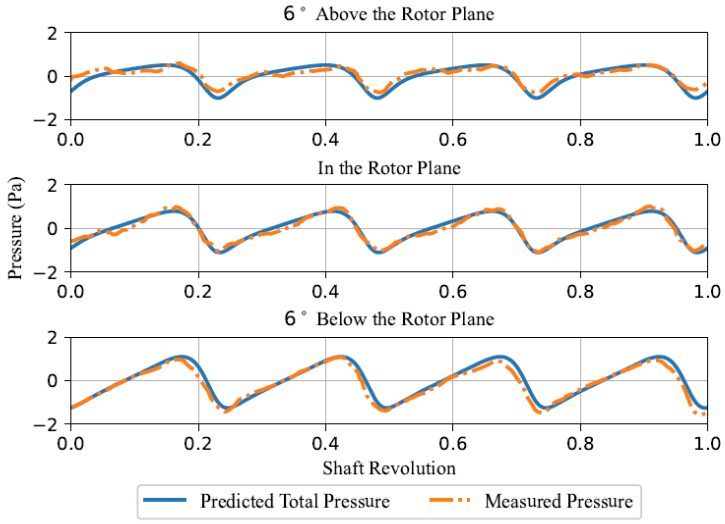

Figure 3.9. Predicted and measured data of scaled Boeing Model 360 [38].

Table 3.2 Parameters of geometry used for the BPM validation [76].

	Parameter	Value
Geometry	R(m)	0.1588
	c/R	0.20
	$\boldsymbol{\theta_{tip}}(°)$	7
	$\boldsymbol{N_b}$	4
	$\boldsymbol{\sigma}$	0.255
Operating Condition	$\boldsymbol{C_T}$	0.0131
	$\boldsymbol{M_{tip}}$	0.27
	Ω_c **(RPM)**	5417

The broadband noise prediction was validated by comparing the spectral contents between

results of PSU-WOPWOP and Pettingill and Zawodny [77]. The parameters of the geometry were provided by [76], which are listed in Table 3.2.

In addition, this blade was designed to have an ideal twist to simplify the process of validation. The BPM method was chosen for the broadband noise prediction because the Pegg model [73] was developed for helicopters rather than multirotor aircraft, and instead of predicting individual broadband noise sources, it shows them combined together, which would make it impossible to find the dominant noise sources [27].

While employing the BPM model for the research [27], the condition of a fully-tripped boundary layer was utilized because it led to better agreement between the prediction and experimental data [27], [76], [78]. LBL-VS noise was disregarded in the noise prediction because it would give erroneous results when applied to the case of a tripped boundary layer [27], [76].

Output files that contain information about geometry, airloads, operating condition, and broadband inputs were provided by VSPWOPWOP and used as input files to PSU-WOPWOP for validation. As shown in Figure 3.10 [27], similarities between results from PSU-WOPWOP, NASA software, and experimental data (i.e., total broadband noise) can be observed. However, the discrepancy is examined in the bluntness noise, which is approximately 6 dB at the peak, is assumed to be the result of the default setting [27]. Specifically, 0.5 mm and 14° were used for trailing edge bluntness and trailing edge included angle, respectively. However, the actual values for these parameters are 0.8 mm and 16° [27], [76]. Despite this difference, the results match well with results from the NASA prediction and experimental data. From this, it was assumed that the noise prediction system can be employed for broadband noise prediction of the multicopter.

With this coupled system of OpenVSP, VSP2WOPWOP (or CHARM) and PSU-WOPWOP, the far-field distance of urban air mobility was studied.

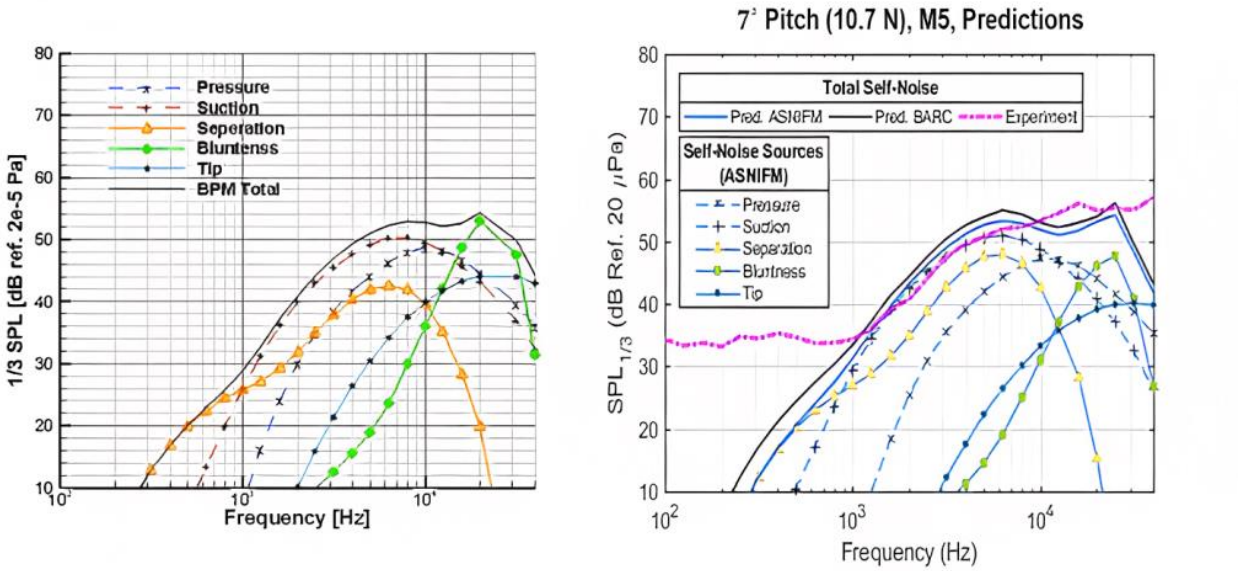

(a) PSU-WOPWOP Predictions. (b) NASA Predictions.

Figure 3.10. Comparison between PSU-WOPWOP and NASA software [27].

Chapter 4

Far-field Distance for UAM

4.1 Technical Approach

A computational approach to determining the acoustic far-field of unconventional rotorcraft will be developed and applied to models of several different aircraft. These computer models predict the acoustic pressure amplitude for a range of observers at various distances from the center of the aircraft. The rate of amplitude decay can then be found by comparing the amplitude at different distances. The amplitude decay is compared to spherical spreading across a range of distances, allowing the extent of the acoustic far-field to be determined.

This procedure is applied to several different aircraft configurations to investigate the effect of configuration changes on the far-field distance. First, the procedure is applied to a conventional helicopter main rotor to establish that the predicted results are consistent with the conventional wisdom for helicopters. Next, the approach is applied to a small multirotor UAS in hover. The rotor RPM, number of rotors, and vehicle size are varied in order to investigate the effect on the far-field distance. Finally, the procedure is applied to a generic model of a passenger carrying lift+cruise eVTOl aircraft in both hover and forward flight.

The conventional helicopter main rotor modeled in this thesis is an approximation of the Sikrosky S-76 (see Figure 4.1). The S-76 main rotor has a dimeter of 13.4 m and rotates at

Figure 4.1 S-76D helicopter [79].

approximately 288 RPM.

The small UAS (sUAS) aircraft configurations investigated in this thesis are variations on the Tarot X8 octocopter, shown in Figure 4.2, which has been the subject of extensive outdoor acoustic measurements conducted by Penn State [66]. The rotor blades have a diameter of 0.381 m, an aspect ratio ($R/\bar{c}$) of 8, a linear taper ratio of 0.32, a constant thickness to chord ratio of 0.03, an assumed ideal twist distribution and a solidity (σ) of 0.08. Each rotor has two blades. The rotor blade pitch was set to maintain a thrust of 4.2 N on each rotor. Variations on the baseline configuration considered in this thesis include the rotation rates (4000 and 6000 RPM), number of rotors (1, 4, 6, and 8) and rotor arm lengths (0.7 *D*, 2.1 *D*, and 3.5 *D*).

Figure 4.2 Tarot X8 octocopter sUAS [66].

The final configuration considered is a generic lift+cruise eVTOL design with four lifting rotors

and pusher propeller, as shown in Figure 4.3. All rotors on the generic eVTOL are 0.52 m in diameter. The wingspan is 6.35 m, roughly 3.6 *D*. The length of the vehicle is 7.42 m long (roughly 4.3 *D*). The far-field distance procedure is applied to this aircraft in both hover and low speed forward flight. The generic eVTOL design provides an initial look at the far-field distance characteristics of passenger carrying multirotor aircraft.[2]

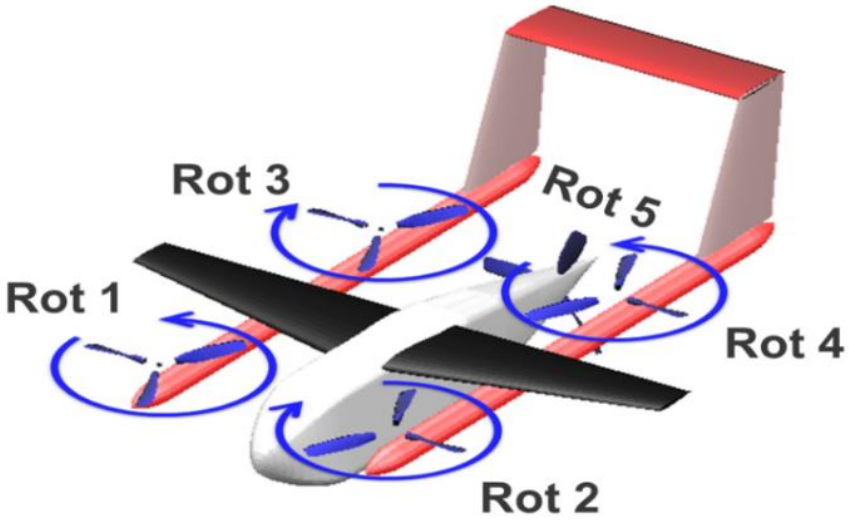

Figure 4.3 Generic lift+cruise eVTOL [35].

4.2 Determination of the Far-Field Distance

This section describes the procedures used to determine the far-field distance in this thesis. The far-field distance for the sUAS configurations were examined by predicting the acoustic field on a series of 14 noise hemispheres with radii ranging from approximately 2.5 to 300 rotor diameters, centered on the centroid of the rotors (see Figure 4.4). The radii of the spheres were chosen to vary logarithmically. Observers on each hemisphere were spaced with 5-degree increments in both azimuth and elevation angle, resulting in 1297 observers for each hemisphere.

[2] Damaris Zachos did the setup and performed all the computations for the generic eVTOL and S-76 helicopter. The method for determining the far-field distance was the work of the author [35].

For a single azimuth and elevation angle, the noise predicted at the 14 radii were compared with a scaling of the noise from the farthest distance to the other radii using the *1/r* law (i.e., spherical spreading). The change in SPL between two distances due to the *1/r* law is described by:

$$SPL_2 = SPL_1 - \left|20 \log_{10} \frac{D_2}{D_1}\right| \tag{4.1}$$

where SPL_1 and SPL_2 are the SPL levels at the first and second distances, and D_2/D_1 is the ratio between the two distances.

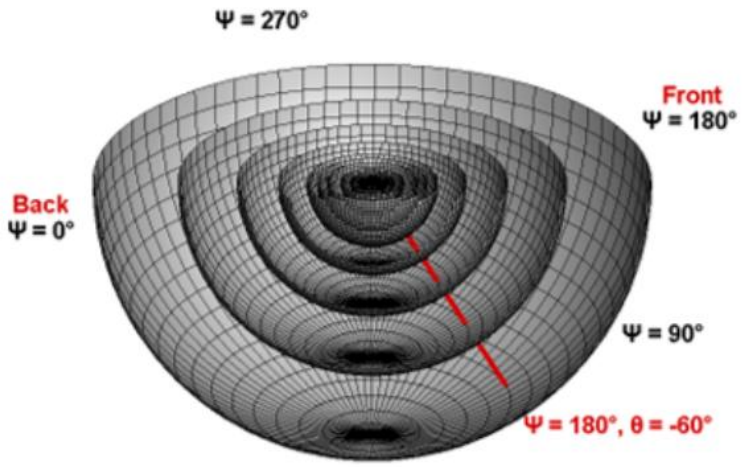

Figure 4.4 Schematic of noise hemispheres used for far-field distance determination [35].

The difference between the *1/r* law SPL and results of PSU-WOPWOP (Δ SPL) was assessed to determine the far-field distance. The criterion used is $|\Delta SPL| \leq x$, where x is the selected tolerance. This process was repeated in all directions on the noise hemisphere. For example, Figure 4.5a shows the far-field determination for a single Tarot X8 rotor operating at 4000 rotations per minute (RPM). The observer is located at azimuth angle ψ = 180° and elevation angle θ = −60°, as shown in Figure 4.4. The acoustic far-field is approximately 5.5 rotor diameters when the far-field tolerance criterion is set to 0.3 dB (i.e., x = 0.3 dB). The difference

between spherical spreading and the PSU-WOPWOP predictions is shown in Figure 4.5b. In both figures in Figure 4.5, the small circle indicated the distance (in rotor diameters) where the criterion is first met. Note that since the observers are placed at fixed radial locations, the actual difference between the predictions and spherical spreading may be somewhat less than the tolerance at this point. Since the criteria of 0.3 dB showed satisfactory results in multiple observer directions, this tolerance value was used for all sUAS analyses in this thesis.

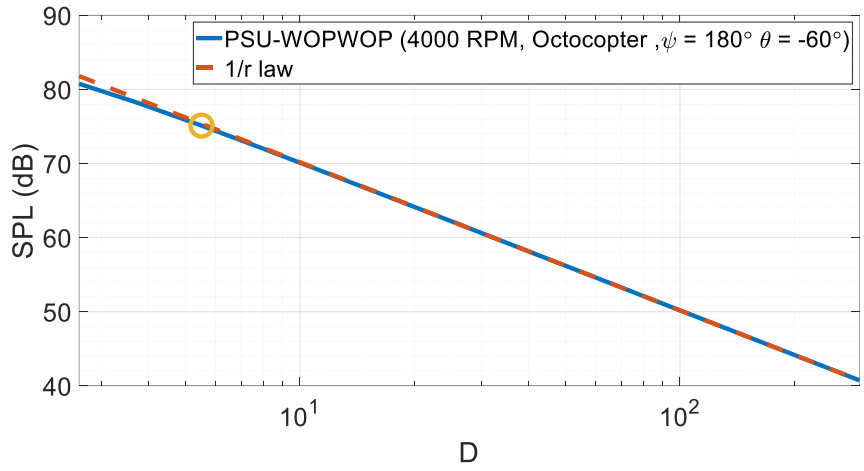

(a) SPL comparison between PSU-WOPWOP and 1/r law.

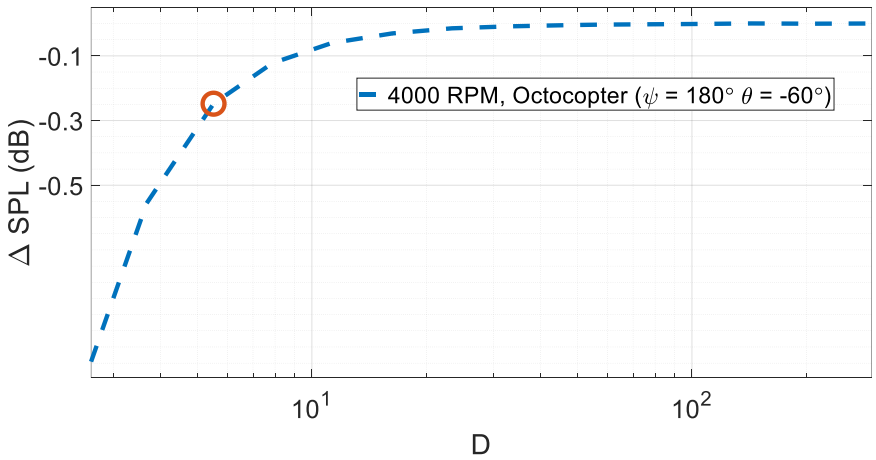

(b) ΔSPL according to D.

Figure 4.5. Far-field distance determination at azimuth ψ = 180° and elevation = −60° [35].

After the far-field distances are computed for all directions, they are plotted on a stereographic

projection of the hemisphere to show the directivity of the far-field distance. Figure 4.6 shows the coordinate system of the stereographic projection used to plot hemisphere in this thesis.

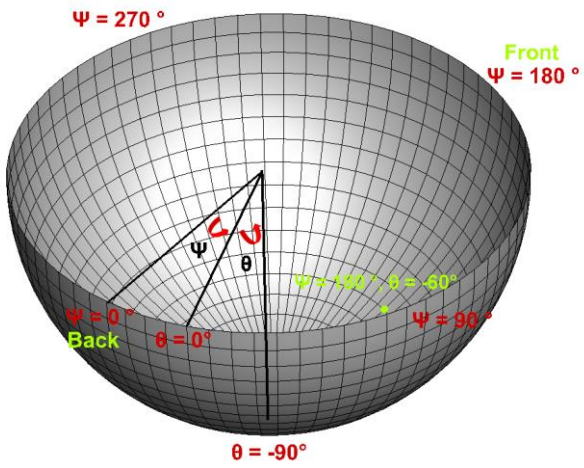

(a) Noise hemisphere.

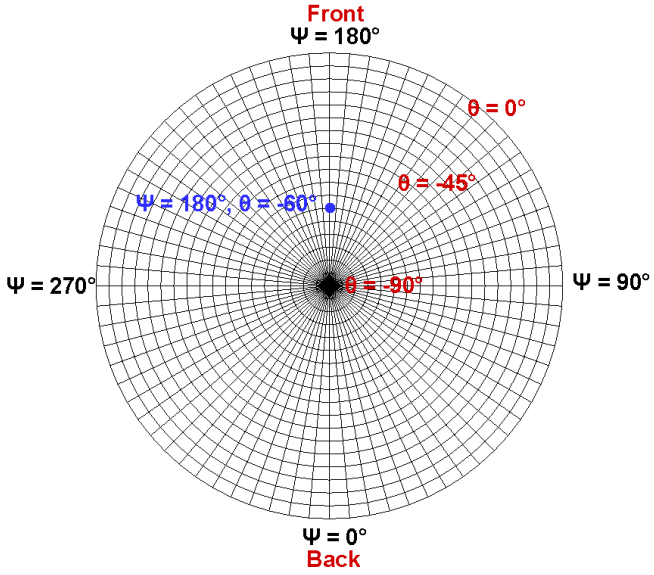

(a) Stereographic projection of noise hemisphere.

Figure 4.6. Noise hemisphere and stereographic projection [35].

The far-field was determined in a similar way for the S-76 and generic eVTOL models. Figure

4.7 shows three overall sound pressure level (OASPL) hemisphere predictions at various distances for the main rotor of an S-76 The amplitudes have been normalized to 100 rotor diameters via Eqn 1. There is a small change in directivity of the noise between the noise at 1.5 *D* in Figure 4.7a and that a 5 *D* in Figure 4.7b. The high amplitude lobe at $\psi = 40°$ and $\theta = -45°$ in Figure 4.7a has shifted forward slightly, to $\psi = 85°$ in Figure 4.7b. The region of low noise in 1.5 *D* (Figure 4.7a) has also shifted forward in the 5 *D* hemisphere. This implies that the 1.5 *D* hemisphere is within the near field of the helicopter. The 5 *D* hemisphere, shown in Figure 4.7b, has essentially identical directivity and magnitude of the far-field distance as the 100 *D* hemisphere, shown in Figure 4.7c; therefore, the 5 *D* hemisphere is in the acoustic far-field of the helicopter. This result is in agreement with the 5 *D* "rule of thumb" for the far-field distance for helicopters.

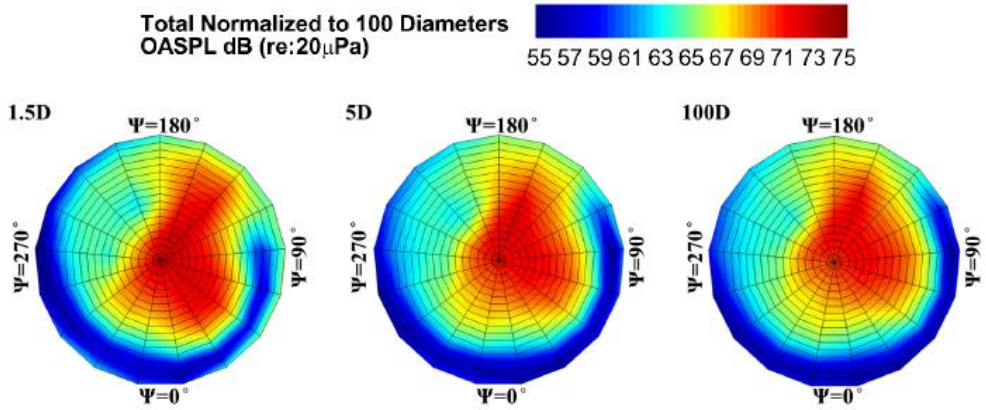

(a) Near field (1.5 *D*). (b) Far field (5 *D*). (c) Far field at a greater distance (100 *D*).

Figure 4.7. S-76 noise hemisphere for a level flight, 80 knot operating condition at different distances normalized to 100 diameters [35].

The same approach used to determine the directivity of the far-field distance for the sUAS was also applied to the S-76, although a smaller set of hemisphere radii were used. Figure 4.8b shows the comparison for a single location on the hemisphere. If the tolerance criteria of 0.3 dB used for the UAS is also used for the S-76, the far-field of the S-76 will be identified at approximately

50 *D* from the main rotor hub. However, if the criteria is relaxed to 1.0 dB, as defined in ISO standard 3745 [80] and applied to rotors by Turkdogru and Ahuja [33], then the far-field exists near the 5 *D* rule of thumb for conventional helicopters. For this reason, the 1.0 dB criteria is used for the larger vehicles.

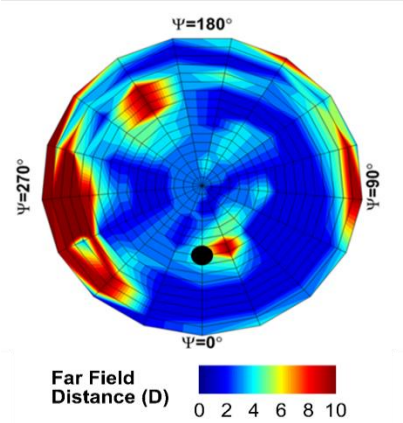

(a) S-76 normalized far field determination using a 1.0 dB tolerance (normalized by rotor diameter *D*).

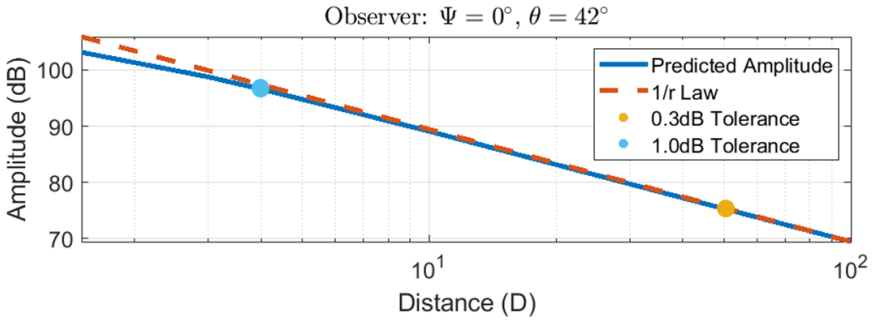

(b) Far field determination at out of plane observer (black dot in Figure 4.6a).

Figure 4.8. Far field determination for S-76. 80 knots level flight **[35]**.

The far-field distance for a range of observer locations is shown in Figure 4.8a. On average, the far-field starts at 3.8 *D* when a tolerance of 1.0 dB is used. The dark red regions contain values between 10 *D* and 50 *D*. Overall, this method matches conventional wisdom that the far-field of a helicopter starts around 5 rotor diameters in most directions. The same method, with a 1.0 dB

tolerance criterion, was used for determining the far-field of a crewed generic eVTOL later in this thesis.

4.3 Results

The approach described in the previous section was applied to two types of aircraft. First, a parametric study was conducted on a variety of sUAS configurations based on the Tarot X8 to understand how configuration changes affect the far-field distance. Then, the approach is applied to a higher fidelity simulation of a larger lift+cruise eVTOL aircraft. This aircraft is evaluated in both hover and forward flight in order to vary the effect of aerodynamic interactions between the rotors that may affect the far-field distance. A comparison between the sUAS and lift+cruise eVTOL studies is then made to evaluate similarities and differences between the far-field characteristics of each aircraft.

4.3.1 Change in Far-Field Distance with Number of Rotors

In this subsection, the effect of the number of rotors on the far-field distance of a sUAS is evaluated. Single rotor, quadcopter, hexacopter, and octocopter configurations are analyzed. In all cases, the gap between rotors was set to 0.05 rotor diameters. The rotors for each configurations were placed as shown in Figure 4.9. The curved arrow represents the direction of the rotation.

The relative importance of the tonal and broadband noise sources is expected to vary with tip Mach number, as shown in Figure 4.10 [29]. For that reason, the rotation rates of the rotors were also varied from 4000 RPM to 6000 RPM, with tip Mach numbers of 0.23 and 0.35, respectively.

4.3.1.1 *4000 RPM*

Stereographic projections of the predicted hover noise hemispheres for the octocopter configuration are shown in Figure 4.11 on a hemisphere of radius 33 D for both the broadband self noise (Figure 4.11a) and the total of broadband and tonal noise sources (Figure 4.11b). There

are no significant differences between the noise hemispheres, suggesting that the OASPL is dominated by the broadband noise sources. The directivity is axisymmetric relative about the vertical axis of the aircraft, even though contributions of multiple rotors are included, since the broadband noise generated by each rotor is added incoherently.

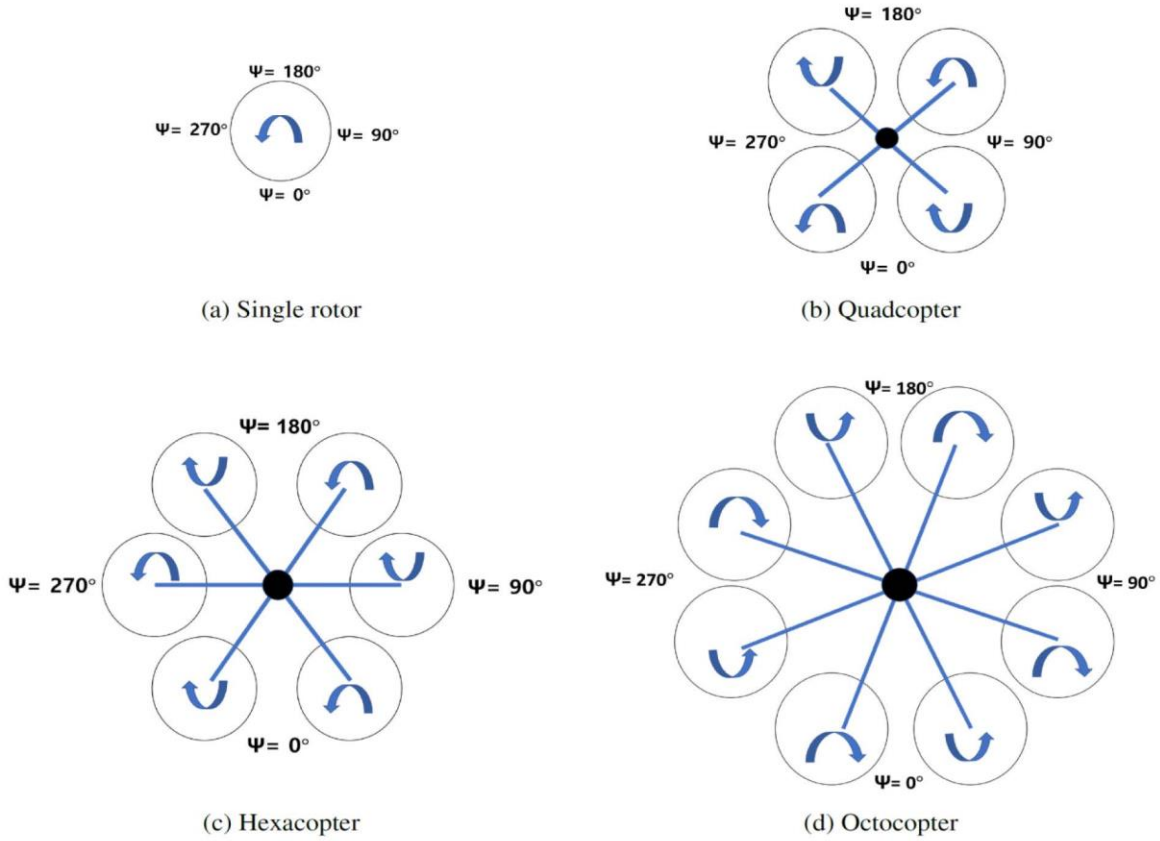

Figure 4.9. sUAS configuration [35].

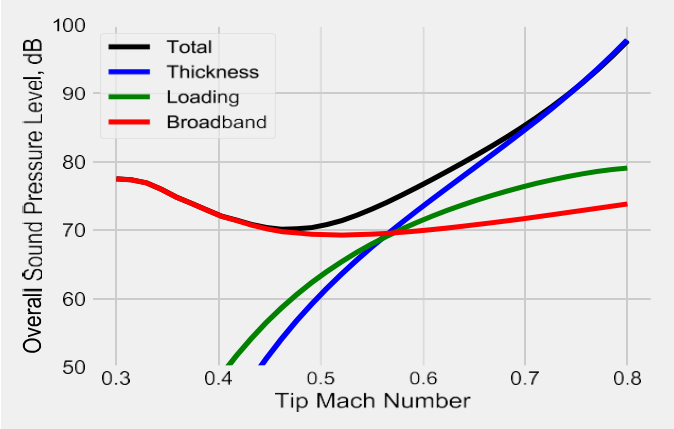

Figure 4.10. Predicted variation in in-plane noise levels by source mechanism for a generic UAM rotor [29].

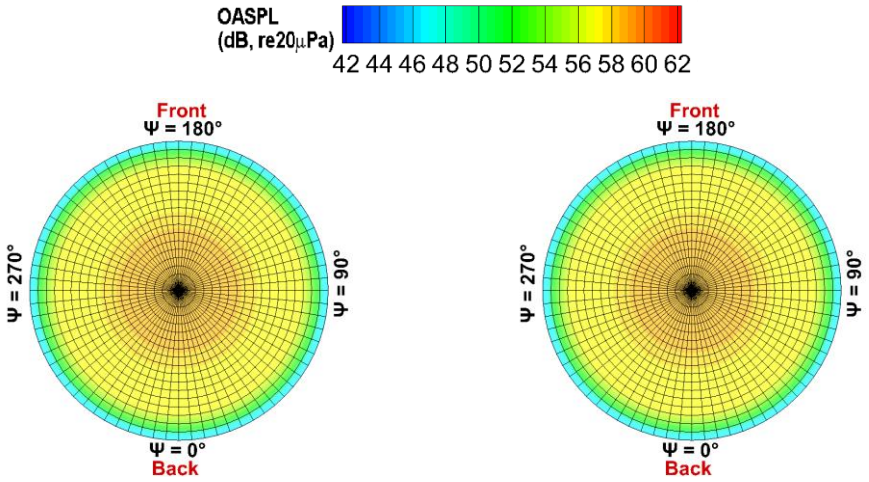

(a) Broadband noise. (b) All noise components.

Figure 4.11. Comparison between OASPL for broadband and all noise components (tonal and broadband) for the octocopter in hover at 4000 RPM [35].

Figure 4.12 shows the predicted OASPL hemispheres for both near and far fields, with the noise levels normalized to a fixed radius of 100 diameters using spherical spreading. Noise hemispheres are shown for both a single rotor (Figures 4.12a and 4.12b) and an octocopter (Figures 4.12c and 4.12d). Notably, the differences between the near- and far-field hemispehres are greater for the octocopter than they are for a single rotor. In the single rotor case, Figures 4.12c and 4.12d have very similar OASPL everywhere; whereas for the octocopter case, the

OASPL levels are very difference near the rotor plane (i.e., θ near 0°). Specifically, in the octocopter near-field case (shown in Figure 4.12c) the values of OASPL for observers near the rotor plane is approximately 62 dB, while in the far-field case (shown in Figure 4.12d), the values of OASPL for observers near the rotor plane is approximately 42 dB. The larger difference between near- and far-field OASPL hemispheres indicates the average value of the far-field distance of the octocopter might be larger than for the single rotor case. Another thing to note in Figure 4.12 (compare Figures 4.12a and 4.12c, or Figures 4.12b and 4.12d) is the difference in the far-field OASPL below the rotor for single rotor and octocopter is about 9 dB, which is the increase expected for three incoherence source doubling (i.e., incoherent addition for broadband noise).

Figure 4.13 shows the far-field distance determined for each UAS configuration, normalized by rotor diameter. A pattern that resembles a ring an elevation angle of approximately $\theta = -40°$ appears for the multirotor configurations. This ring indicates that the far-field has the smallest extent near $\theta = -40°$, increasing as the elevation angle is increased or decreased. This phenomenon is not explained by the behavior of the OASPL hemisphere in Figure 4.11b, since the predicted OASPL amplitude increases monotonically with decreasing elevation angle.

A more detailed inspection of the far-field determination method was thus conducted. The fall off in noise levels with distance for an observer located at $\theta = -40°$ was inspected for the octocopter case, shown in Figure 4.14. As shown, the far-field distance was found to be 2.6 D at an observer positioned at $\psi = 30°$ and $\theta = -40°$. The slope of the predicted amplitude at this ψ and θ combination matches the spherical spreading slope after the identified far-field distance. Therefore, the nearby far-field distance determined around $\theta = -40°$ in Figure 4.14 is a realistic determination of the far-field.

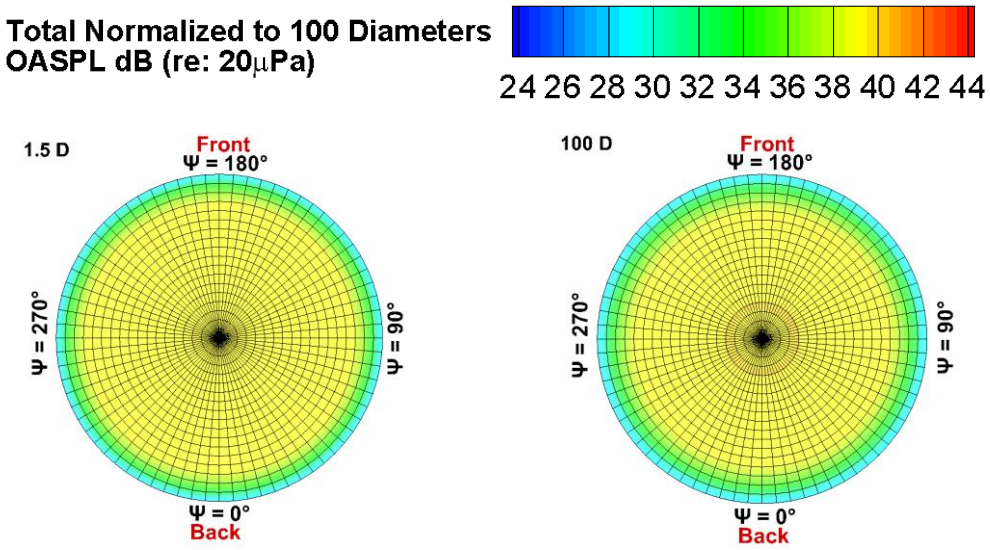

(a) Single rotor, near field.

(b) Single rotor, far field.

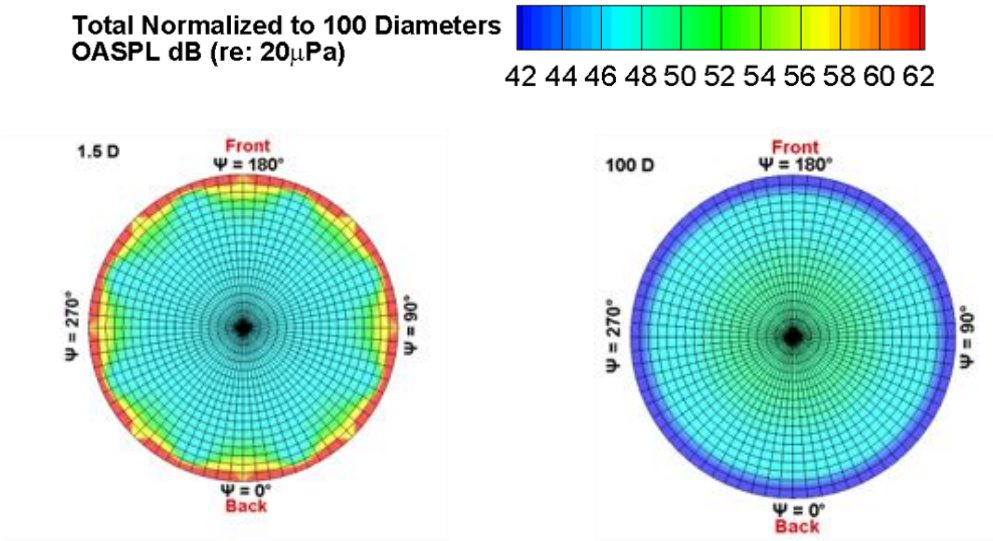

(c) Octocopter, near field.

(d) Octocopter, far field.

Figure 4.12. sUAS OASPL hemispheres normalized to 100 *D*. Hover at 4000 RPM [35].

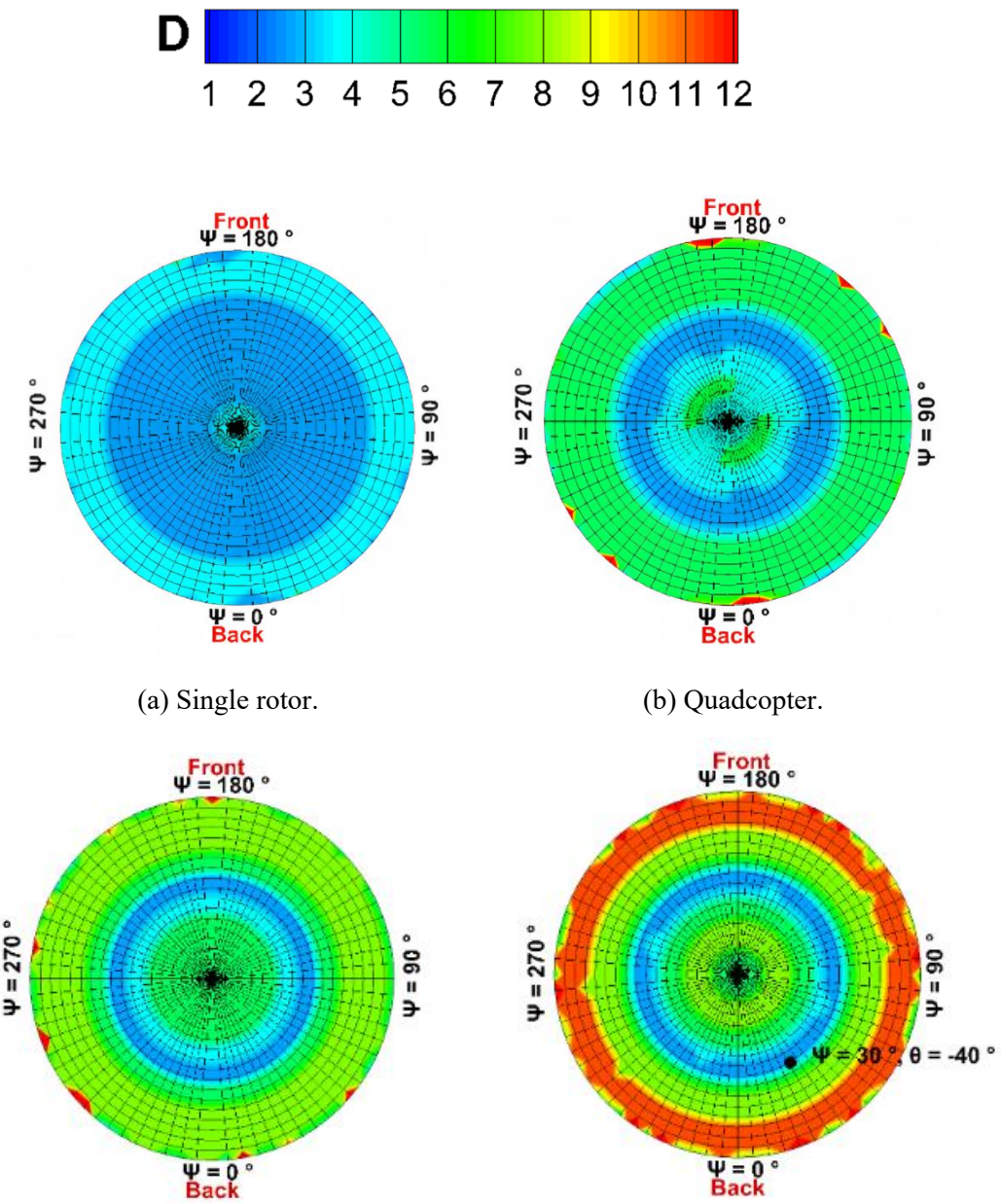

(a) Single rotor.

(b) Quadcopter.

(c) Hexacopter.

(d) Octocopter.

Figure 4.13. Normalized far-field distance directivity for sUAS configurations with varying numbers of rotors (normalized by rotor diameter *D*). Hover at 4000 RPM [35].

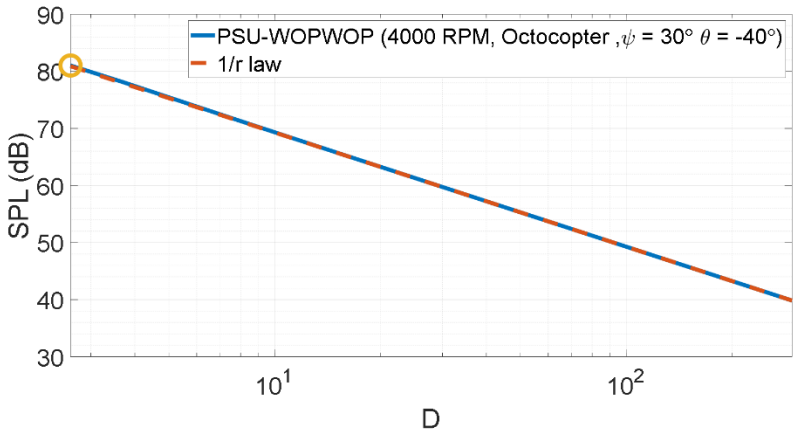

Figure 4.14. Predicted SPL decay vs. distance along $\psi = 30°$ and $\theta = -40°$ for the octocopter configuration in hover at 4000 RPM [35].

In Figure 4.15, the far-field distance is re-normalized by vehicle diameter D_v instead of the rotor diameter D as was done in Figure 4.13. The vehicle diameter D_v is the diameter of a circle that circumscribed all the rotors. The values of D_v for each configuration is given in Table 4.1. Although the directivity of the far-field in Figure 4.15 appears somewhat different than shown in Figure 4.13, these differences are solely due to changes in the contour levels because the same normalization is applied in all directions. Of more importance is that the normalization of the far-field distance by D_v results in very similar normalized far-field distances for all the multirotor vehicles (compare Figures 4.15b to 4.15d).

There is a relation between the number of rotors and far-field distance, as shown in Table 4.2. As the number of rotor increases, the distance of the far-field also increases. However, it should be noted that when the radii of the noise hemispheres are normalized by the diameter of the vehicle (shown in Table 4.1), the far-field distance converges to approximately 1.8 D_v as shown in Table 4.3. The differences between the minimum and maximum values of the far-field distance are smaller when normalized by vehicle diameter instead of the rotor diameter. In other words, the far-field distance may scale better with vehicle size than rotor diameter for similar small multicopter aircraft with different numbers of rotors.

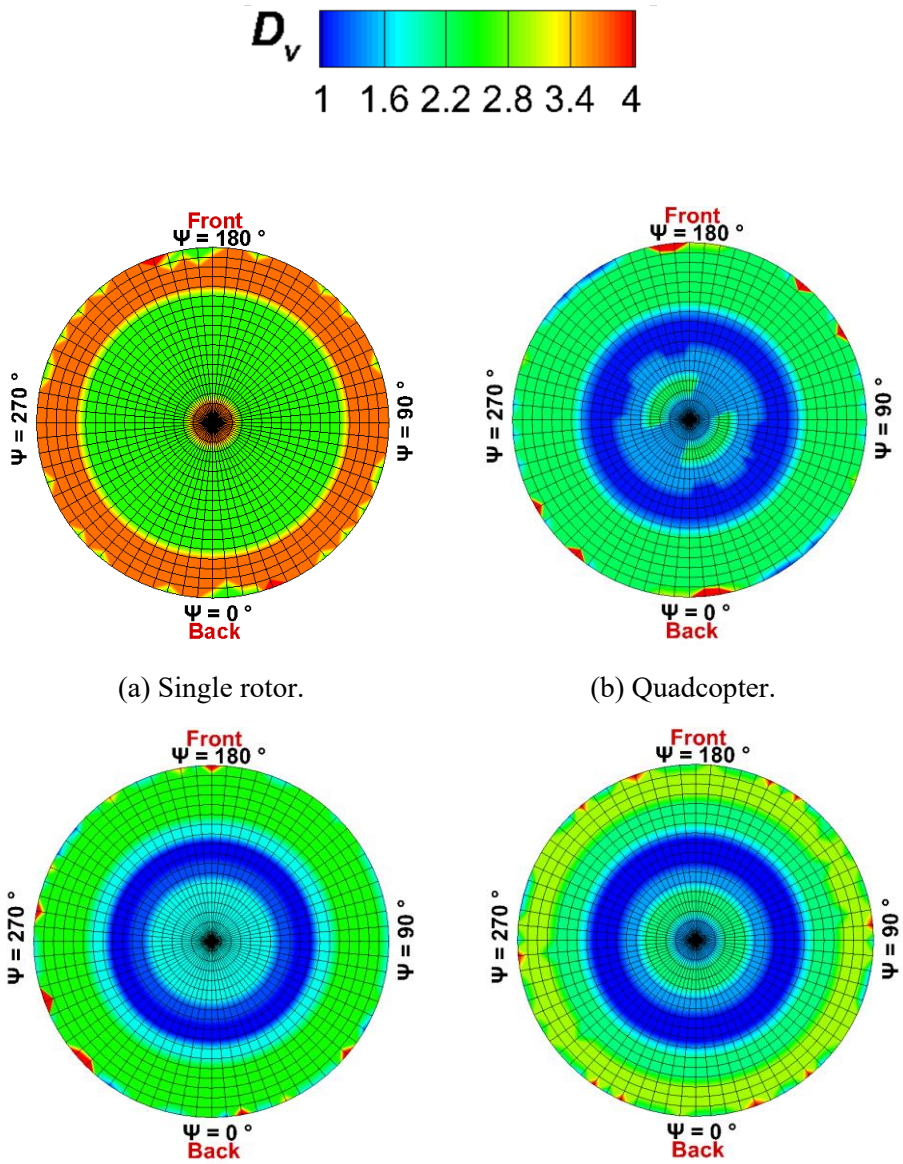

(a) Single rotor. (b) Quadcopter.

(c) Hexacopter. (d) Octocopter.

Figure 4.15. Normalized far-field distance directivity for sUAS configurations with varying numbers of rotors (normalized by vehicle diameter D_v). Hover at 4000 RPM [35].

Table 4.1. Vehicle diameter (Change in far-field distance with number of rotors).

Number of rotors	D_v (m)
1	0.381
4	0.95
6	1.18
8	1.43

Table 4.2. Summary of 4000 RPM Tarot drone far-field distance. Normalized by D.

Number of Rotors	Min/Max (D)	Average (D)
1	2.6/3.7	3.0
4	2.6/5.5	4.2
6	2.6/7.9	5.7
8	2.6/11.3	6.9

Table 4.3. Summary of 4000 RPM Tarot drone far-field distance. Normalized by D_v.

Number of Rotors	Min/Max(D_v)	Average(D_v)
1	2.6/3.7	3.0
4	1.1/2.2	1.7
6	0.8/2.5	1.8
8	0.7/3.0	1.8

4.3.1.2 *6000 RPM*

The same configuration study was performed with a rotation rate of 6000 RPM. This increase in RPM corresponds to an increase in tip Mach number. Recall that the tip Mach number influences the relative importance of the different noise generation mechanisms. Despite the increase in RPM, broadband noise is still dominant as shown for the octocopter configuration in Figure 4.16. Broadband noise also remained the dominant noise source for the other multicopter configurations when the RPM was increased to 6000 RPM.

As with the 4000 RPM case, the average value of the normalized far-field distance increases with number of rotors (See Table 4.4). Likewise, the normalized far-field distance converges for the multicopter configurations when the distance is normalized by vehicle diameter, D_v, as shown in Table 4.5. In fact, the average far-field distance normalized by vehicle diameter D_v in the 6000 RPM case ($\approx$ 1.5, see Table 4.5) is close to the value found in the 4000 RPM case ($\approx$ 1.8, see Table 4.3).

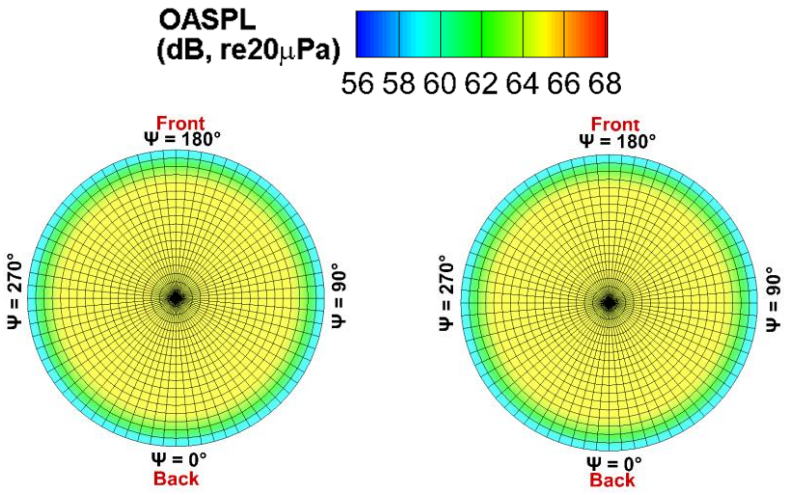

(a) Broadband noise. (b) All noise components.

Figure 4.16. Comparison between OASPL for broadband and all noise components (tonal and broadband) for the octocopter in hover at 6000 RPM [35].

Table 4.4. Summary of 6000 RPM Tarot drone far-field distance. Normalized by D

Number of Rotors	Min/Max (D)	Average(D)
1	2.6/5.5	3.0
4	2.6/7.9	3.7
6	2.6/7.9	4.5
8	2.6/7.9	5.6

Table 4.5. Summary of 6000 RPM Tarot drone far-field distance. Normalized by D_v.

Number of Rotors	Min/Max(D_v)	Average(D_v)
1	2.6/5.5	3.0
4	1.1/3.2	1.5
6	0.8/2.5	1.5
8	0.7/2.1	1.5

The normalized far-field distance for all configurations at 6000 RPM (normalized by vehicle diameter) is shown in Figure 4.17. The directional dependence of the far-field distance is significantly different from that found for 4000 RPM (see Figure 4.15). The axisymmetry of the far-field distance found in the 4000 RPM cases is no longer present when the rotation rate

is increased to 6000 RPM. By increasing the rotation rate, there is now a periodic azimuthal variation that changes with the number of rotors. The acoustic interference between the rotors is known to affect the directivity of the tonal noise produced, as found by Smith et al. in their rotor phase study [81] and by Pascioni et al. in their rotor phase studies [82]. But in Figure 4.17, the broadband noise is dominant and is not expected to have significant azimuthal variation. Further study is needed to fully understand the results in Figure 4.17.

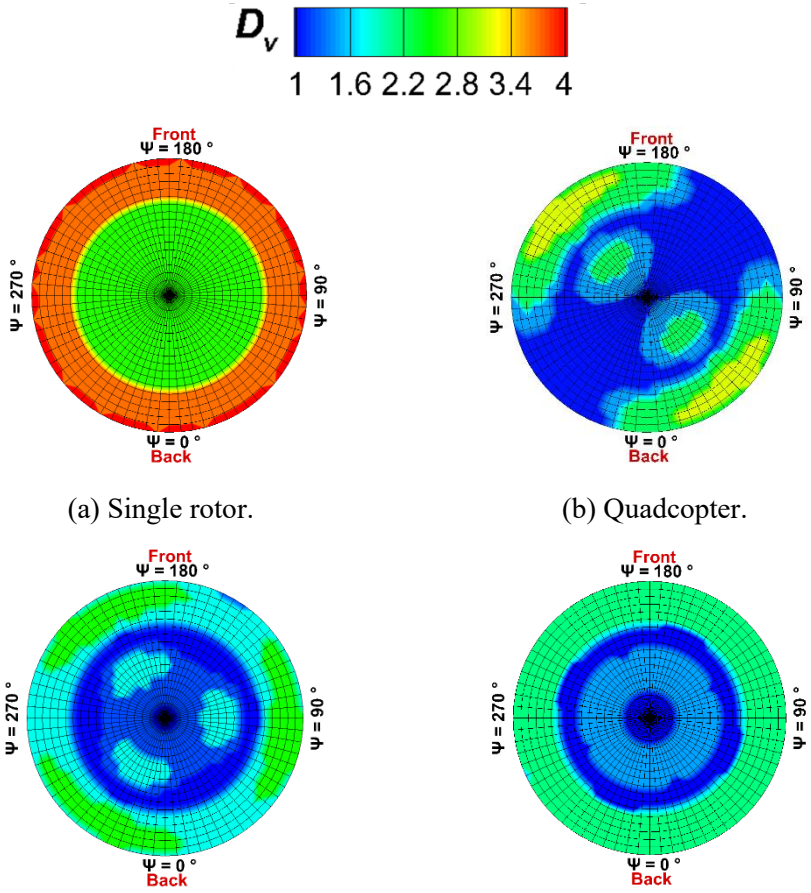

(a) Single rotor. (b) Quadcopter.

(c) Hexacopter. (d) Octocopter.

Figure 4.17. Far field distance directivities, 6000 RPM. Distance normalized by D_v [35].

4.3.2 Change in Far-Field Distance with Vehicle Size

The previous results suggest that normalizing the far-field distance by the vehicle diameter, rather than the rotor diameter may provide a more consistent determination of the far-field

distance for multirotor sUAS. To further investigate this relationship, the arm lengths of the quadcopter model was varied to see how the far-field distance varies. The rotor arm lengths were set to values of 0.7 D, 2.1 D, and 3.5 D. In previous sections, the arm lengths of 0.7 D were used for the case of the quadcopter. This results in a corresponding change to the diameter of the vehicle, as summarized in Table 4.6.

Table 4.6. Diameter of vehicle (Change in far-field distance with vehicle size).

Arm Length	D_v (m)
0.7 D	0.95
2.1 D	2.00
3.5 D	3.08

For this study, the rotor rotation rate is set to 4000 RPM. Therefore, broadband noise is dominant. As shown in Figure 4.18 (noise hemisphere with a radius of 33 D), the noise levels and axisymmetric broadband directivity seen for the baseline arm length, shown in Figure 4.11, are maintained for all other arm lengths.

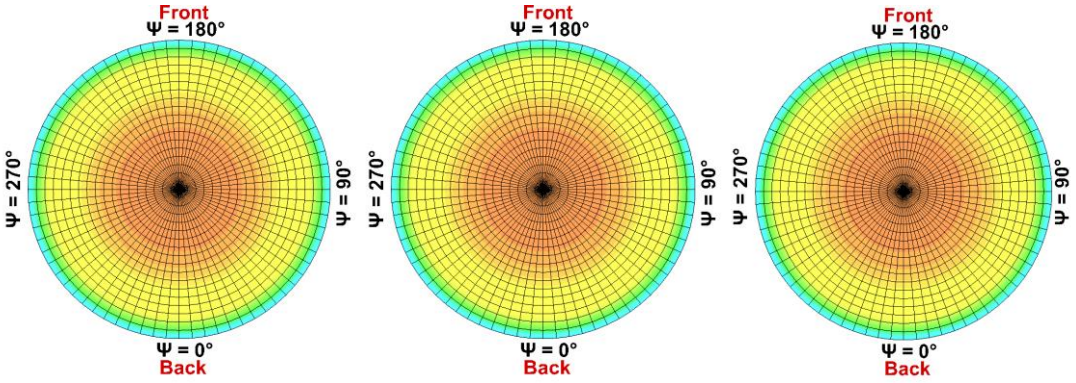

(a) 0.7 D. (b) 2.1 D. (c) 3.5 D.

Figure 4.18. OASPL noise hemispheres for a quadcopter as the rotor arm length is varied [35].

Using the far-field distance determination approach, the variation in the far-field distance with observer angle was computed for all three arm lengths. Figure 4.19 plots the variation

normalized to the rotor diameter, whereas Figure 4.20 plots the variation normalized to the vehicle diameter. Once again, the directivity of the far-field is generally axisymmetric and a ring of low far-field distances at an elevation angle $\theta = -40°$for all arm lengths simulated. When comparing the distances normalized by rotor diameter (Figure 4.19), it is readily apparent that normalizing by vehicle diameter provides a closer agreement in the far-field distance between configurations with different arm lengths.

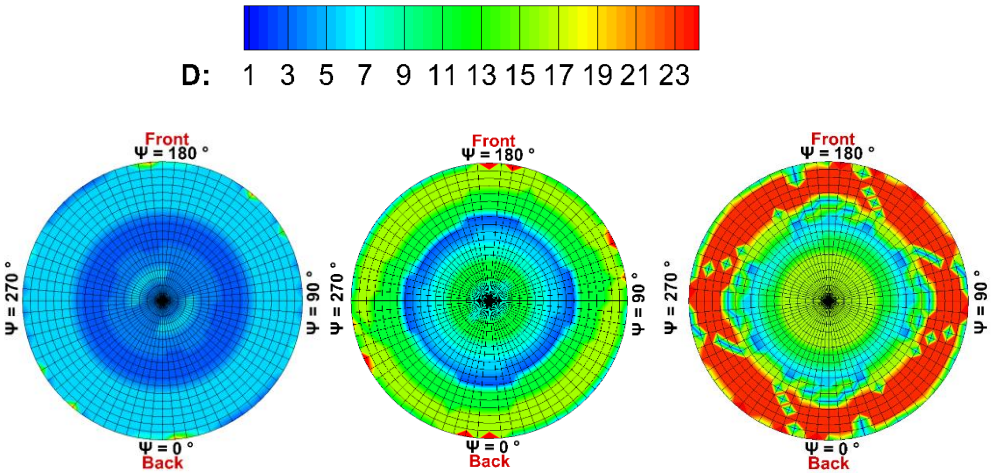

(a) 0.7 D. (b) 2.1 D. (c) 3.5 D.

Figure 4.19. Far field distance directivities, vehicle studies. Distance normalized by D [35].

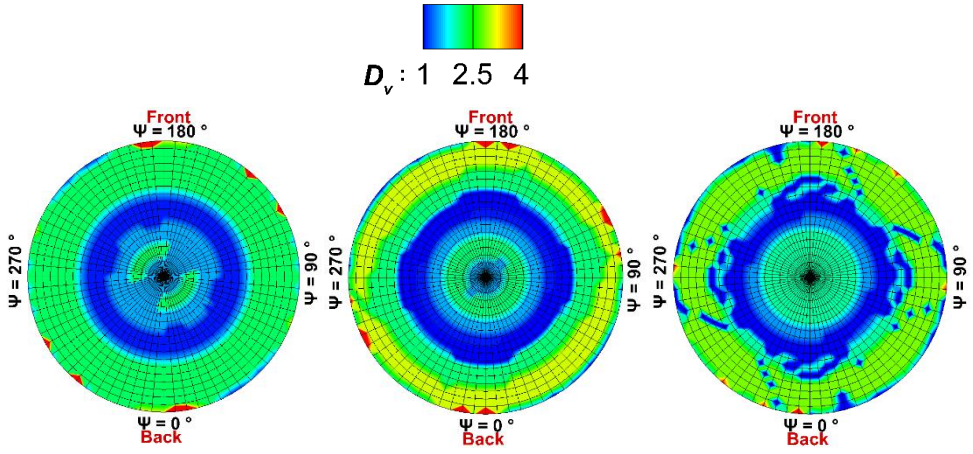

(a) 0.7 D. (b) 2.1 D. (c) 3.5 D.

Figure 4.20. Far field distance directivities, vehicle size studies. Distance normalized by D_v [35].

The far-field distance variations with arm length are summarized in Table 4.7 (normalized by

rotor diameter, D) and Table 4.8 (normalized by vehicle diameter, D_v). Once again, normalizing by vehicle diameter causes closer agreement between vehicles with different rotor arm lengths. Specifically, the average far-field distance in rotor diameters varies between 4.2 D and 15.9 D, but this range is reduced to 1.7 D_v to 2.0 D_v when normalized by vehicle diameter. Altogether, the results of both configuration studies indicate that it may be possible to develop a consistent rule of thumb for the far-field distance of small multirotor UAS having similar rotors. However, this scaling may not hold as the configuration and operating conditions of the rotors change with the scale of the aircraft, e.g., from sUAS to larger multirotor aircraft designed for UAM operations.

Table 4.7. Summary of vehicle size studies Tarot drone far-field distance. Normalized by D.

Arm Length	Min/Max (D)	Average (D)
0.7 D	2.6/5.5	4.2
2.1 D	3.7/16.3	10.0
3.5 D	5.5/23.4	15.9

Table 4.8. Summary of vehicle size studies Tarot drone far-field distance. Normalized by D_v.

Arm Length	Min/Max(D_v)	Average(D_v)
0.7 D	1.1/2.2	1.7
2.1 D	0.7/3.1	1.9
3.5 D	0.7/2.9	2.0

4.3.3 Application to Larger Aircraft

The parametric study described previously demonstrated that a consistent rule for the far-field distance could be established across a wide range of multirotor sUAS configurations. However, sUAS vary significantly from larger crewed multirotor aircraft, both in terms of the size of the vehicle and the aerodynamic operating conditions of the rotors during flight. In this section, the far-field distance characterization approach will be applied to a higher fidelity simulation of a generic lift+cruise eVTOL concept (previously shown in Figure 4.4) to investigate these

differences.

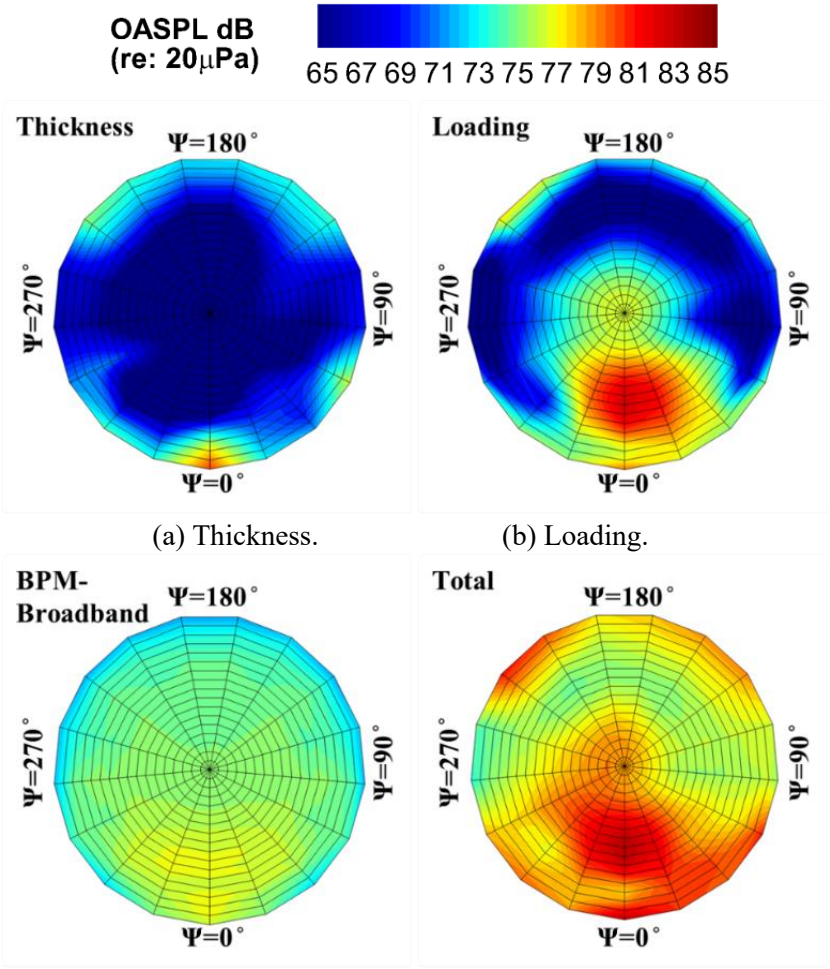

(a) Thickness. (b) Loading.

(c) Broadband. (b) Total noise.

Figure 4.21. Contributions of each noise source component to the unweighted OASPL for the generic eVTOL in hover [35].

As mentioned previously, the rotors of the larger eVTOL aircraft operate at different conditions than the sUAS; in particular, they are more highly loaded and operate at higher tip Mach numbers. Consequently, the relative importance of the different noise generation mechanisms may differ from the sUAS configurations. The predicted OASPL for noise components (thickness, loading, and broadband) and the total noise for the generic lift+cruise eVTOl is shown in Figure 4.21 on a 10 rotor diameter (i.e., 10 D) hemisphere. Thickness noise levels are low compared to loading and broadband noise components. Loading noise is responsible for the hot spots in the total noise level hemisphere (near the rear of the vehicle, $\psi \approx 0°$, below the

propeller), while broadband noise is the most significant contributor in other directions. This differs from the sUAS configurations, where broadband noise was dominant in all directions.

4.3.3.1 *Far-Field Distance in Hover*

In this section, the far-field distance of the eVTOL aircraft is investigated in a hovering flight condition. First, the near- and far-field noise levels are compared for a single rotor. Figure 4.22 shows the near and far-field directivity patterns of one of the rotors for the generic eVTOL (rotor 2, on the front left side). For both hemispheres, the noise levels were normalized to a 100 rotor diameters using spherical spreading (Eqn 1). The near field plot has a hemisphere radius of 3 *D*. The far-field plot hemisphere radius is 10 *D*. First, notice that the OASPL is not axisymmetric as one might expect for an isolated hovering rotor. The asymmetry visible in Figure 4.22 caused by the relatively small interaction between the rotors installed on the eVTOL. Although the noise is computed for only one rotor (i.e., rotor 2), the aerodynamic loads on the rotor are from a full vehicle aerodynamics computation, as can be seen in the lack of axisymmetry. Second, the normalized noise levels and their directivity change as the observer is moved from the near-field to the far-field. Figure 4.23 shows a similar comparison of the near- (i.e., 5 *D*) and far- (i.e., 10 *D*) field OASPL directivity for the entire aircraft, including all rotors and the propeller. The noise directivity of the full aircraft model is different than that of the single rotor, because it has multiple “hotspots”.

Next, the far-field determination method was applied to both the single rotor and full aircraft model of the eVTOL aircraft. Figure 4.24a shows the normalized far-field distance hemisphere for the single rotor, normalized by the rotor diameter. The average distance for the far-field to develop is 12 *D*, with values over the hemisphere ranging from 3 to 30 *D*. The average value is twice that of the 5 *D* “rule of thumb” often used for conventional helicopters and about three times the average far-field distance found for S-76 main rotor model.

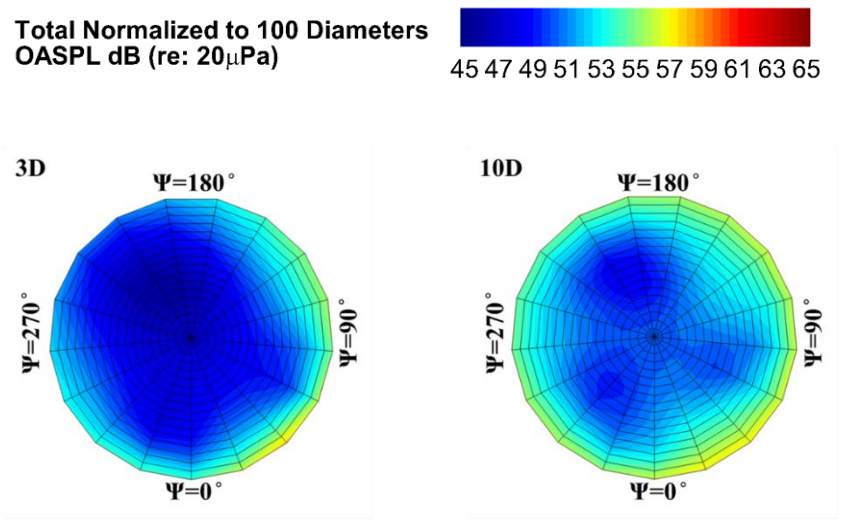

(a) Near field. (b) Far field.

Figure 4.22. Single eVTOL rotor (i.e., rotor 2) noise hemipsheres for hover at near- and far-field normalized to 100 D [35].

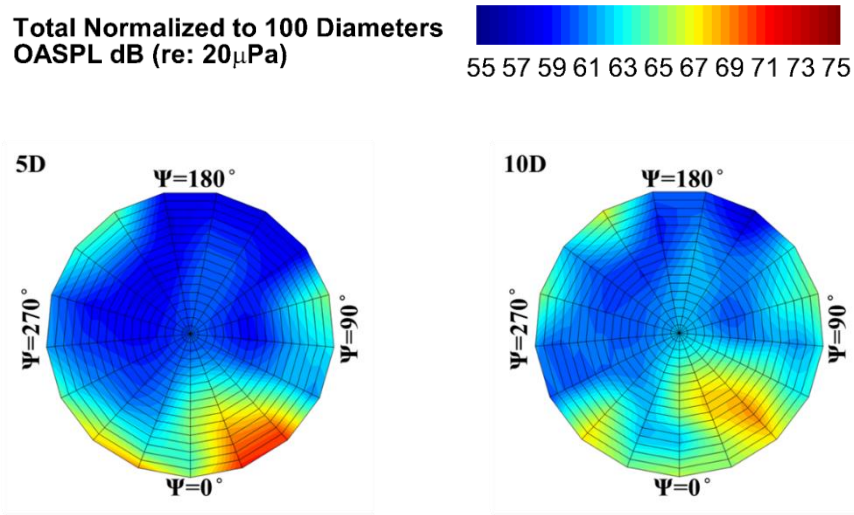

(a) Near field. (b) Far field.

Figure 4.23. Complete eVTOL aircraft noise hemispheres for hover at near- and far-field distances normalized to 100 D [35].

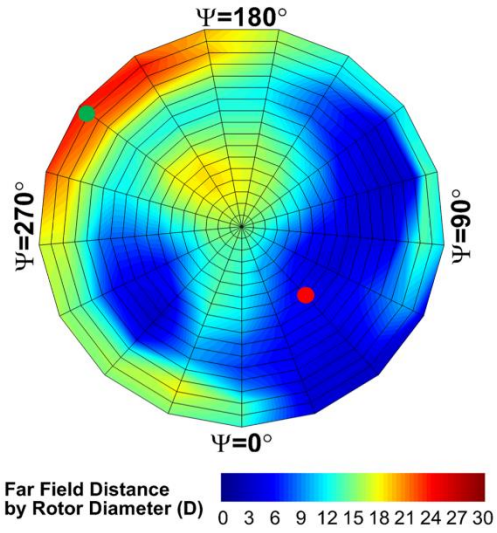

(a) Normalized far-field distance directivity.

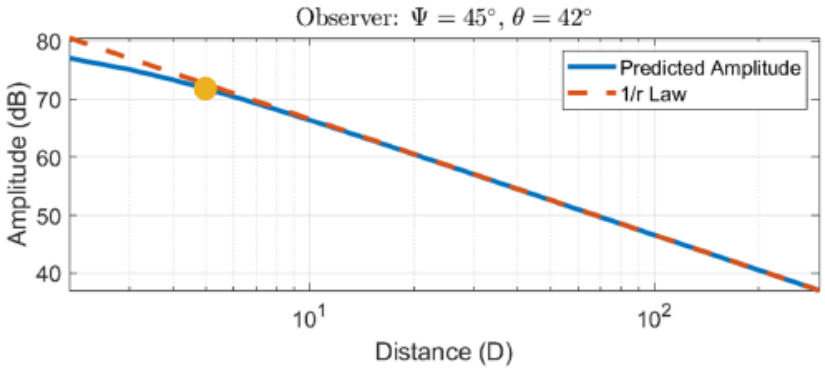

(b) Far-field determination for an out-of-plane direction. Red dot location in Figure 4.24a.

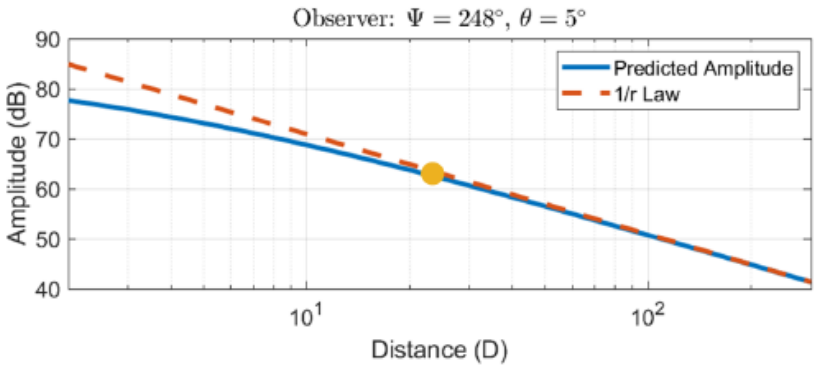

(c) Far-field determination for a near-in-plane direction. Green dot location in Figure 4.24a.

Figure 4.24. Far-field distance determination for a single eVTOL rotor in hover [35]

The predicted decay in noise levels with distance is compared to the *1/r* law for out-of-plane (see Figure 4.24b) and near-in-plane (see Figure 4.24c) observer directions. The out-of-plane and in-plane directions are marked in Figure 4.24a with red and green dots, respectively. For the out-of-plane direction shown in Figure 4.24b the onset of the far-field is close to the aircraft, approximately 6 *D*. However, for an observer located near the plane of the rotor (see Figure 4.24c), the predicted decay does not converge to spherical spreading until a further distance (i.e., 25 *D*).

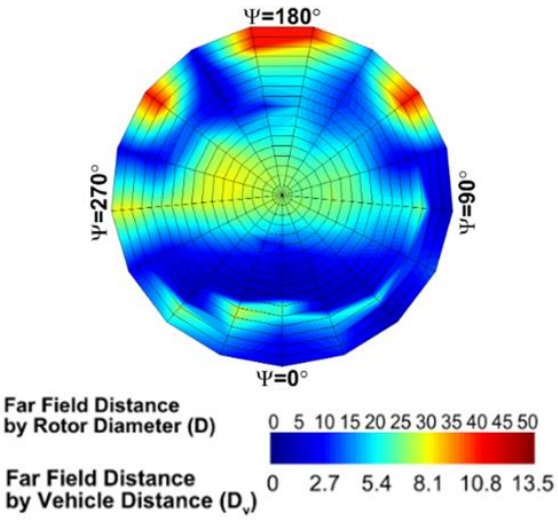

Figure 4.25 Normalized far field distance directivity, hovering, full vehicle [35].

Next, Figure 4.25 shows the far-field distance directivity for the complete aircraft, normalized by rotor diameter D = 1.71 m or vehicle diameter D_v = 6.37 m, as indicated by the two different legends. Guided by the earlier definition of vehicle diameter, for the generic eVTOL the vehicle diameter D_v is defined as the diameter of a sphere that circumscribes the vehicle, which is the longest dimension of the vehicle. The directivity of the normalized far-field distance differs from that of the isolated rotor. When the rotor diameter is used for normalization, there are regions where the far-field does not develop for more than 30 *D* around $\theta = 0°$; $\psi = 180°$, 115°, and 245°. On average, the full aircraft far-field develops near 22 *D*, which is twice that of the single rotor model. When the vehicle diameter is used for normalization, the average full aircraft far-

field is about 5.9 D_v.

These results may be compared to the small quadcopter UAS configuration evaluated previously. The average far-field distance normalized by vehicle diameter for the small quadcopter was 1.7 D_v, whereas that normalized distance for the generic eVTOL was 5.9 D_v. The vehicle diameter normalization of the far-field distance still results in values that are similar to the rule of thumb for helicopters, but it is somewhat different for the two different size vehicle classes. This may be due to the difference in ranking of the noise components (thickness, loading, and broadband) for the different operating conditions. Nevertheless, these results indicate that establishing a *single* guideline for the far-field distance of multirotor aircraft across different scales may not be feasible.

4.3.3.2 *Far-Field Distance in Forward Flight*

The previous sections of this thesis focused on the far-field determination in hover. However, forward light changes the operating condition of the rotors, which affects their noise generation and may similarly affect the acoustic far-field. In this section, the generic lift+cruise eVTOL is analyzed in a low-speed 50 knots level flight condition. The condition was selected because it represents a transition flight condition where the lifting rotors and the propeller are all operating.

As with the hover cases, a comparison between the predicted near- and far-field noise levels was conducted for both a single rotor and complete aircraft. Figure 4.26 show the predicted OASPL in the near (i.e., 2 *D*) and the far (i.e., 10 *D*) fields, as determined by visual inspection, for the eVTOL rotor 2 in forward flight. Once again, a significant difference is seen in both the magnitude and directivity of the noise between the near and far-fields for the single rotor. Figure 4.27 shows the same plots for the full aircraft model. The near field plot radius is 5 *D*. The far-field plot is 10 *D*. Here, the changes in directivity are even more apparent, with multiple "hotspots" forming as the observers move into the far-field.

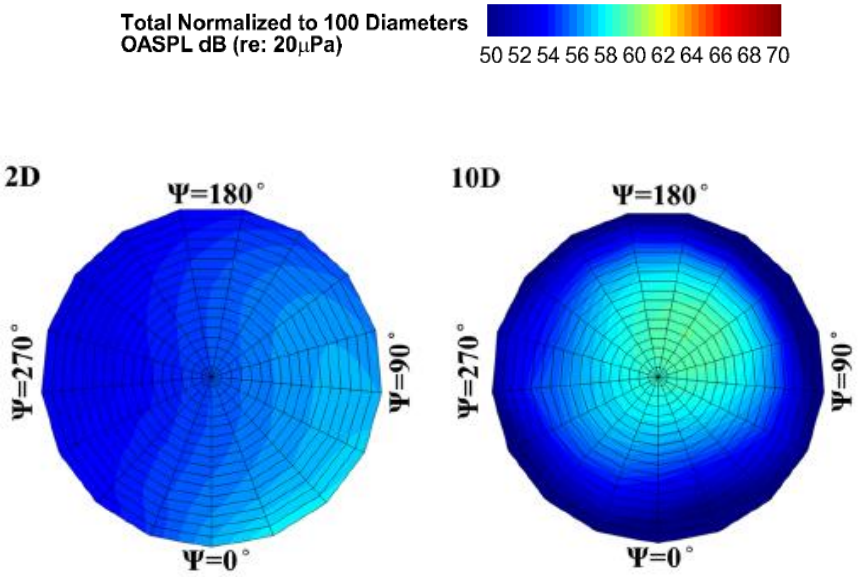

(a) Near field (b) Far field

Figure 4.26 Single eVTOL rotor (rotor 2) noise hemispheres for 50 knots level flight at near- and far-field distances normalized to 100 rotor diameters. [35].

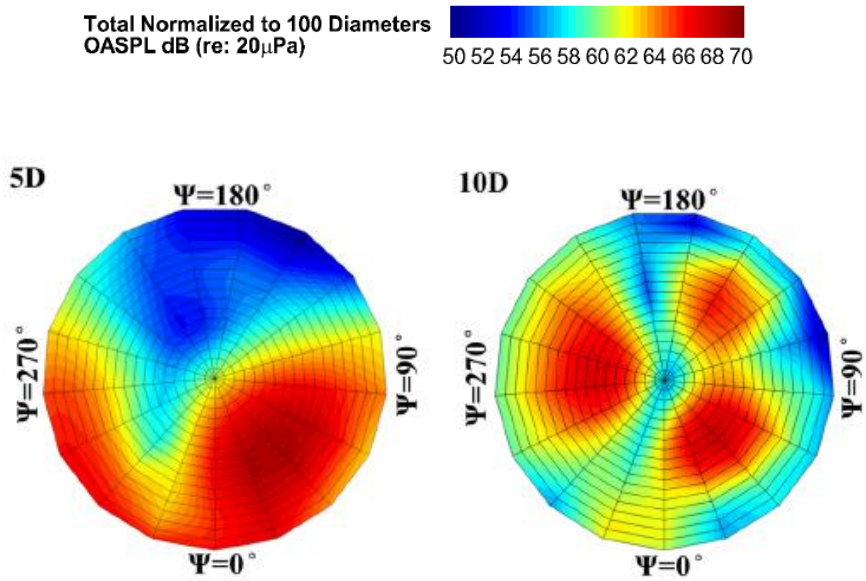

(a) Near field (b) Far field

Figure 4.27 Complete eVTOL aircraft noise hemispheres for 50 knots level flight at near- and far-field distances normalized to 100 rotor diameters. [35].

The far-field distance determined for rotor 2 in forward flight is shown in Figure 4.28. As with the far-field distance predictions for the full aircraft in hover, there are hotspots where the far-field distance is high. On average, the far-field of rotor 2 in 50 knots forward flight is 11 *D*, similar to the average hover value. However, the directivity of the far-field differs from that of the hover condition. Appearing similar to the sUAS results, a "ring" of low far-field distances develops at an elevation angle approximately 45 degrees below the plane of the rotors. To better understand this "ring", the decay in noise levels is plotted for three elevation angles at the same azimuth ($\psi = 0°$) in Figure 4.29. For the observer directly below the aircraft (see Figure 4.29a), the far-field eventually converges to spherical spreading as expected. For the out-of-plane observer at an elevation angle of 42 degrees, the far-field also convers to spherical spreading (see Figure 4.29b), although the decay rate in the near-field region is different than for the observer below the aircraft. For the in-plane observer (see Figure 4.29c), the predictions do not converge to the spherical spreading law in the range of distances considered. Nevertheless, because the predicted noise level curve passes through *1/r* law scaling line, a distance was still identified by the method, leading to an inaccurate determination of the far-field extent. Alternate methods of determining the far-field distance may need to be developed for cases like this, for example, by finding the distance where the rate of decay in the predicted noise level matches that predicted noise levels by spherical spreading.

Applying the procedure to the full aircraft in forward flight results in the far-field distance hemisphere plots in Figure 4.30, normalized by rotor diameter D = 1.71 m or vehicle diameter D_v = 6.37 m, as indicated by the two different legends. The average far-field distance for the generic eVTOL model at 50 knots in level flight is 20.2 D or 5.4 D_v. For a majority of the observers on this hemisphere, the far-field has developed within D_v. However, there are directions where far-field distance is much farther away than the average value. The regions denoted by dark red indicate those directions near the plane of the rotor where the far-field does not develop. Examination of the noise level decay at along one of these directions (directly

behind the aircraft, see Figure 4.31) shows that the predictions do eventually converge to the rate of decay predicted by spherical spreading.

The average far-field distance for the hover and forward flight conditions of the generic eVTOL are summarized in Table 4.9. For both the single rotor and the full aircraft cases, the average far-field distance is comparable between hover and forward flight. Therefore, the change in the flight condition of the aircraft does not appear to significantly affect the onset of the far-field, at least for this vehicle and these flight conditions. This should be explored further to confirm this hypothesis.

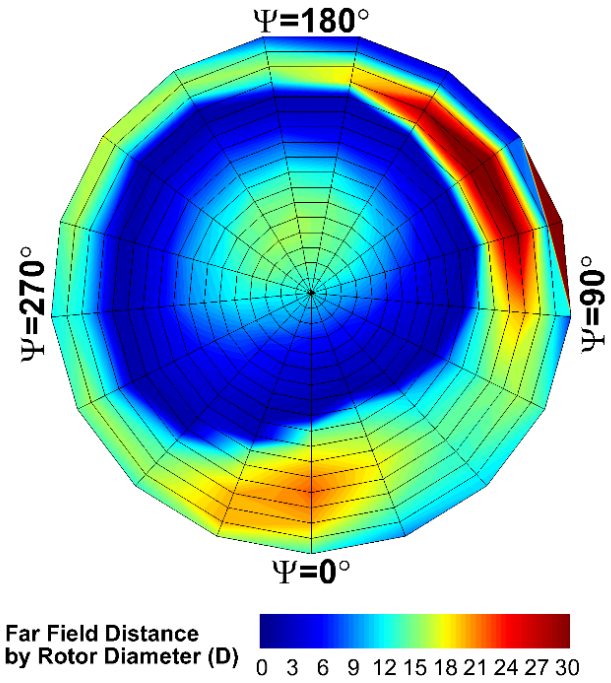

Figure 4.28. Normalized far-field distance hemisphere for generic eVTOL rotor 2 in 50 knots level flight (normalized by rotor diameter *D*). [35].

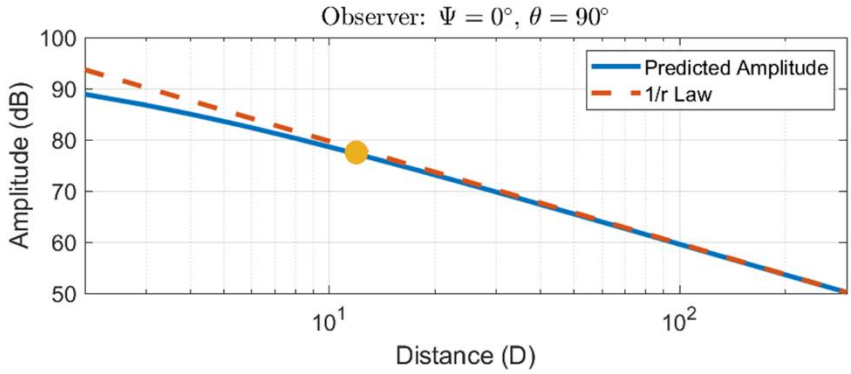

(a) Directly below aircraft.

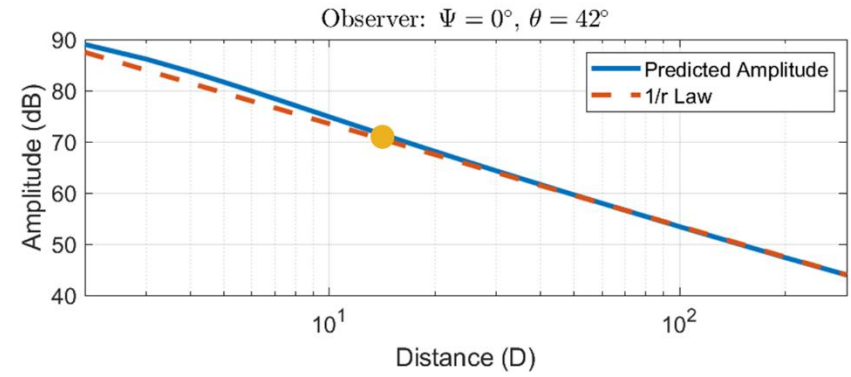

(b) Out-of-plane direction.

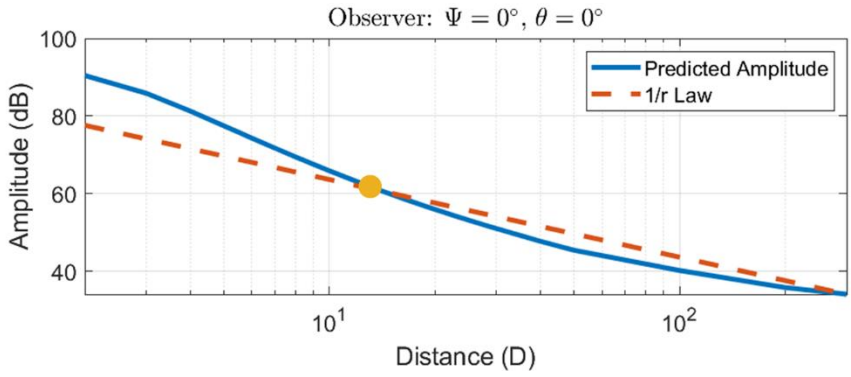

(c) In-plane direction.

Figure 4.29. Predicted decay in noise levels along several directions for the generic eVTOL rotor 2 in 50 knots level flight [35].

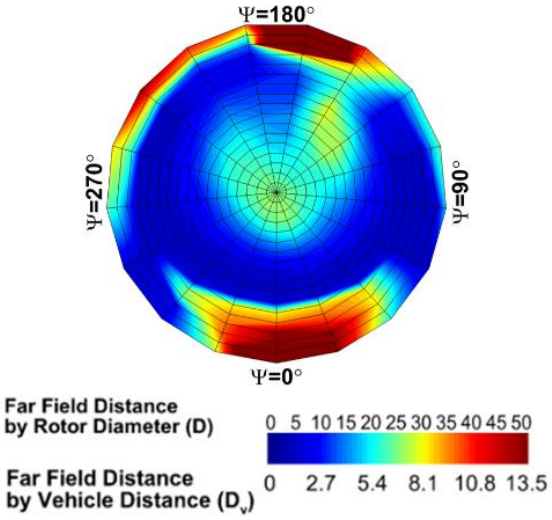

Figure 4.30. Normalized far-field distance hemisphere for generic eVTOL rotor 2 in 50 knots level flight (normalized by rotor diameter *D*) [35].

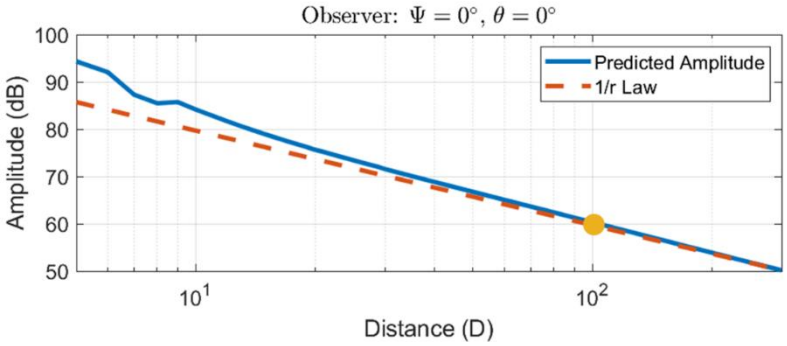

Figure 4.31. Predicted decay in noise levels for the complete generic eVTOL aircraft in 50 knots level flight. Observer direction behind aircraft and in-plane of lifting rotors. [35].

Table 4.9. Average far-field distances for generic lift+cruise eVTOL rotor and aircraft [35].

Flight condition	Min/Max (D)	Average
Hovering	12 D	22 D / 5.9 D_v
Forward flight	11 D	20.2 D /5.4 D_v

Chapter 5

Conclusions and Future Work

5.1 Conclusions

A computational approach was developed to characterize the far-field distance of multirotor aircraft and this approach was applied to several different models, including an S-76 helicopter main rotor, various sUAS configurations, and a generic eVTOL **[35]**.

Regarding the case of sUAS, configurations were varied to understand the effect of aircraft configuration and operation on the far-field distance and its directivty **[35]**. Although changes in rotor RPM did not affect the far-field distance, when the numbers of rotors and the arm lengths were increased, the proportionality between these parameters and far-field distance was found, assuming that the distance was normalized by the rotor diameter. However, when the distance was normalized by the vehicle diameter, it scaled to range of 1.5 to 2.0 $\boldsymbol{D_v}$. This suggests the possibility of establishing a general rule for the far-field distance of sUAS.

Regarding the generic eVTOL aircraft of the hovering, multiple rotor cases, it was found that the far-field distance is 5.9 $\boldsymbol{D_v}$, which is three times more compared to the case of sUAS. This might be affected by different aerodynamic operating conditions of the rotors on the larger vehicle and suggests that different guidelines will need to be established for different scale

aircraft **[35]**. When the vehicle has a forward velocity of 50 knots, the far-field distance was 5.4 $\boldsymbol{D_v}$. This implies the far-field distance is insensitive to the flight condition but further research should be conducted, and it should be noted that different criteria (see Section 4.2) has been used for the case of generic eVTOL compared to that of a sUAS **[35]**.

5.2 Future Work

This thesis conducted an initial study on the far-field distance of multirotor aircraft. However, additional research is needed to establish far-field measurement criteria for novel aircraft configurations [35].

5.2.1 Experimental Testing

Penn State [66] conducted the experimental study on the small UAM, Tarot X8, and data was gathered during the flight test. However, the data has not been analyzed to investigate the onset of the far field [35]. Therefore, in future studies, the flight test data should be leveraged.

5.2.2 Computational Modeling

Further computational studies should be done for a wider range of eVTOL flight conditions and configurations to establish whether or not a guideline for far field noise measurement can be developed [35]. Although, results showed differences in far-field distance between sUAS and generic eVTOL, this thesis only considered two blade models (i.e., Tarot X8 plastic blade, and generic eVTOL blade). More rotor and vehicle geometries should be studied and the use of even higher fidelity aerodynamics (i.e., CFD) might be required to more fully understand the results this study was not able to answer or address thoroughly.

5.2.3 Slope Method

Finally, while examining the generic eVTOL aircraft [35], for the in-plane observer, it was found that the predictions do not converge to 1/r law after the determination point for cases such as Figure 4.29c. This implies inaccurate results at some locations. Therefore, a different algorithm

to determine the far-field distance might be required, such as using the slope method for the determination of the far-field distance. Specifically, using the rate of decay of noise (i.e., 6 dB per doubling of distance) rather than the difference between the predicted and scaled results may improve the accuracy and robustness of the far-field distance determination method [35].

References

[1] Thipphavong, D.P., Apaza, R., Barmore, B., Battiste, V., Burian, B., Dao, Q., Feary, M., Go, S., Goodrich, K.H., Homola, J. and Idris, H.R., "Urban air mobility airspace integration concepts and considerations." In *2018 Aviation Technology, Integration, and Operations Conference*, p. 3676. 2018.

[2] Afari, S., Mankbadi, R.R. and Golubev, V.V., "Review of Multi-Rotor Noise Prediction Techniques." In *AIAA AVIATION 2022 Forum*, p. 3463. 2022.

[3] National Research Council, *Uninhabited Air Vehicles: Enabling Science for Military Systems*. Vol. 495. National Academies Press, 2000.

[4] Hasan, S., *Urban air mobility (UAM) market study*. No. HQ-E-DAA-TN70296. 2019.

[5] "The high-flying industry: Urban Air Mobility takes off," *Roland Berger*. https://www.rolandberger.com/en/Insights/Publications/The-high-flying-industry-Urban-Air-Mobility-takes-off.html (accessed 8/30/2022).

[6] Schuurman, M.J., Rattanagraikanakorn, B., Kassapoglou, C. and De Breuker, R., "Urban air mobility (UAM) vehicle design considerations to facilitate future accident investigation." In *AIAA Aviation 2019 Forum*, p. 3628. 2019.

[7] Blank, P., Kirrane, S. and Spiekermann, S., "Privacy-aware restricted areas for unmanned aerial systems." *IEEE Security & Privacy* 16, no. 2 (2018): 70-79.

[8] Wang, Y., Xia, H., Yao, Y. and Huang, Y., "Flying Eyes and Hidden Controllers: A Qualitative Study of People's Privacy Perceptions of Civilian Drones in The US." *Proc. Priv. Enhancing Technol.* 2016, no. 3 (2016): 172-190.

[9] Yao, Y., Xia, H., Huang, Y. and Wang, Y., "Free to fly in public spaces: Drone controllers' privacy perceptions and practices." In *Proceedings of the 2017 CHI Conference on Human Factors in Computing Systems*, pp. 6789-6793. 2017.

[10] Cavoukian, A., *Privacy and drones: Unmanned aerial vehicles*. Ontario: Information and Privacy Commissioner of Ontario, Canada, 2012.

[11] Yoo, W., Yu, E. and Jung, J., "Drone delivery: Factors affecting the public's attitude and intention to adopt." *Telematics and Informatics* 35, no. 6 (2018): 1687-1700.

[12] Wu, P.J. and Lin, K.C., "Unstructured big data analytics for retrieving e-commerce logistics knowledge." *Telematics and Informatics* 35, no. 1 (2018): 237-244.

[13] Nentwich, M. and Horváth, D.M., "The vision of delivery drones: Call for a technology assessment perspective." *TATuP-Zeitschrift für Technikfolgenabschätzung in Theorie und Praxis/Journal for Technology Assessment in Theory and Practice* 27, no. 2 (2018): 46-52.

[14] Lin, A., "Use of drone technology on commercial construction projects." (2018).

[15] Crişan, G.C. and Nechita, E., "On a cooperative truck-and-drone delivery system." *Procedia Computer Science* 159 (2019): 38-47.

[16] Obaid, M., Mubin, O., Basedow, C.A., Ünlüer, A.A., Bergström, M.J. and Fjeld, M., "A drone agent to support a clean environment." In *Proceedings of the 3rd International Conference on Human-Agent Interaction*, pp. 55-61. 2015.

[17] Rani, A.L.K.A., Chaudhary, A.M.R.E.S.H., Sinha, N., Mohanty, M. and Chaudhary, R., "Drone: The green technology for future agriculture." *Harit Dhara* 2, no. 1 (2019): 3-6.

[18] Singh, A.P., Singh, S.P., Singh, A., Gupta, S., Raj, V., Kumar, S., Shankar, R. and Kumar, B., "Application of air purifier drone to control air pollutants in domestic and industrial areas." In *2020 International Conference on Electrical and Electronics Engineering (ICE3)*, pp. 676-679. IEEE, 2020.

[19] Devlin, E., "Factors affecting public acceptance of wind turbines in Sweden." *Wind Engineering* 29, no. 6 (2005): 503-511.

[20] Wolsink, M., Sprengers, M., Keuper, A., Pedersen, T.H. and Westra, C.A., "Annoyance from wind turbine noise on sixteen sites in three countries." In *European community wind energy conference*, vol. 271, p. 276. 1993.

[21] Krishnamoorthy, V., "The Drone of Drones: A Preliminary Investigation of Drone Noise and Animal Welfare in New Zealand Sheep." PhD diss., ResearchSpace@ Auckland, 2019.

[22] Christiansen, F., Rojano-Doñate, L., Madsen, P.T. and Bejder, L., "Noise levels of multi-rotor unmanned aerial vehicles with implications for potential underwater impacts on marine mammals." *Frontiers in Marine Science* 3 (2016): 277.

[23] Weimerskirch, H., Prudor, A. and Schull, Q., "Flights of drones over sub-Antarctic seabirds show species-and status-specific behavioural and physiological responses." *Polar Biology* 41 (2018): 259-266.

[24] Schäffer, B., Pieren, R., Heutschi, K., Wunderli, J.M. and Becker, S., "Drone noise emission characteristics and noise effects on humans—a systematic review." *International journal of environmental research and public health* 18, no. 11 (2021): 5940.

[25] Sharma, K., "Incorporating acoustic assessment into the design and analysis of rotorcraft." (2016).

[26] Stephenson, J.H., Watts, M.E., Greenwood, E. and Pascioni, K.A., "Development and validation of generic maneuvering flight noise abatement guidance for helicopters." *Journal of the American Helicopter Society* 67, no. 1 (2022): 1-12.

[27] Gan, Z.F., "Time-Varying Rotor Noise Computations and Analysis of Electric Vertical Take-Off and Landing Aircraft." (2021).

[28] Rizzi, S.A., Huff, D.L., Boyd, D.D., Bent, P., Henderson, B.S., Pascioni, K.A., Sargent, D.C., Josephson, D.L., Marsan, M., He, H.B. and Snider, R., *Urban air mobility noise: Current practice, gaps, and recommendations*. No. NASA/TP-20205007433. 2020.

[29] Greenwood, E., Brentner, K.S., Rau, R.F. and Ted Gan, Z.F., "Challenges and opportunities for low noise electric aircraft." *International Journal of Aeroacoustics* 21, no. 5-7 (2022): 315-381.

[30] Ramos-Romero, C., Green, N., Roberts, S., Clark, C. and Torija, A.J., "Requirements for drone operations to minimise community noise impact." *International Journal of environmental research and public health* 19, no. 15 (2022): 9299.

[31] Tinney, C.E. and Sirohi, J., "Multirotor drone noise at static thrust." *Aiaa Journal* 56, no. 7 (2018): 2816-2826.

[32] Van Treuren, K., Sanchez, R., Wisniewski, C. and Leitch, P., "Acoustically Testing Stock and Modified UAS Propellers in Both the Near and Far Field." In *Turbo Expo: Power for Land, Sea, and Air*, vol. 84058, p. V001T01A001. American Society of Mechanical Engineers, 2020.

[33] Turkdogru, N. and Ahuja, K.K., "Determination of geometric farfield for ducted and unducted rotors." *International Journal of Aeroacoustics* 11, no. 5-6 (2012): 607-627.

[34] Van Treuren, K., Wisniewski, C. and Cinnamon, E., "Near and Far field Noise Decay from a Quadcopter Propeller with and without a leading edge notch." In *Turbo Expo: Power for Land, Sea, and Air*, vol. 50985, p. V001T01A021. American Society of Mechanical Engineers, 2018.

[35] Hur, K., Zachos, D. R., Brentner, K. S., and Greenwood, E., "Determining the Acoustic Far Field for Multirotor Aircraft," Vertical Flight Society Annual Forum & Technology Display Forum, 2023

[36] McDonald, R.A., "Advanced modeling in OpenVSP." In *16th AIAA Aviation Technology, Integration, and Operations Conference*, p. 3282. 2016.

[37] Hahn, A., "Vehicle sketch pad: a parametric geometry modeler for conceptual aircraft design." In *48th AIAA Aerospace Sciences Meeting Including the New Horizons Forum and Aerospace Exposition*, p. 657. 2010.

[38] Weitsman, D. and Greenwood, E., "Parametric study of eVTOL rotor acoustic design trades." In *AIAA Scitech 2021 Forum*, p. 1987. 2021.

[39] Wachspress, D., "BVI noise prediction using a comprehensive rotorcraft analysis." In *AHS International Annual Forum, 57 th, Washington, DC*. 2001.

[40] Wachspress, D.A., Quackenbush, T.R., Boschitsch, A.H., Yu, M.K. and Whitehouse, G.R., "CHARM User's Manual (Version 6.4)." *CDI technical note, Ewing, NJ* (2018).

[41] Wachspress, D.A., Quackenbush, T.R. and Boschitsch, A.H., "First-principles free-vortex wake analysis for helicopters and tiltrotors." In *ANNUAL FORUM PROCEEDINGS-AMERICAN HELICOPTER SOCIETY*, vol. 59, no. 2, pp. 1763-1786. AMERICAN HELICOPTER SOCIETY, INC, 2003.

[42] Botre, M., Brentner, K.S., Horn, J.F. and Wachspress, D., "Validation of helicopter noise prediction system with flight data." In *Vertical Flight Society 75th Annual Forum & Technology Display*, vol. 13. 2019.

[43] Brès, G.A., Brentner, K.S., Perez, G. and Jones, H.E., "Maneuvering rotorcraft noise prediction." *Journal of Sound and Vibration* 275, no. 3-5 (2004): 719-738.

[44] Goldman, B.A., "Modifications to PSU-WOPWOP for enhanced noise prediction capabilities." (2013).

[45] Leishman, G.J., *Principles of helicopter aerodynamics with CD extra*. Cambridge university press, 2006.

[46] Lighthill, M.J., "On sound generated aerodynamically I. General theory." *Proceedings of the Royal Society of London. Series A. Mathematical and Physical Sciences* 211, no. 1107 (1952): 564-587.

[47] Lighthill, M.J., "On sound generated aerodynamically II. Turbulence as a source of sound." *Proceedings of the Royal Society of London. Series A. Mathematical and Physical Sciences* 222, no. 1148 (1954): 1-32.

[48] Ffowcs Williams, J.E. and Hawkings, D.L., "Sound generation by turbulence and surfaces in arbitrary motion." *Philosophical Transactions of the Royal Society of London. Series A, Mathematical and Physical Sciences* 264, no. 1151 (1969): 321-342.

[49] Brentner, K.S. and Farassat, F., "Modeling aerodynamically generated sound of helicopter rotors." *Progress in aerospace sciences* 39, no. 2-3 (2003): 83-120.

[50] Farassat, F. and Succi, G.P., "The prediction of helicopter rotor discrete frequency noise." *In: American Helicopter Society* (1982): 497-507.

[51] Brooks, T.F. and Burley, C.L., "Blade wake interaction noise for a main rotor." *Journal of the American helicopter Society* 49, no. 1 (2004): 11-27.

[52] Lopes, L.V., Boyd Jr, D.D., Nark, D.M. and Wiedemann, K.E., "Identification of spurious signals from permeable Ffowcs Williams and Hawkings surfaces." In *American Helicopter Society (AHS) International Annual Forum and Technology Display*, no. NF1676L-25336. 2017.

[53] Spalart, P.R., Belyaev, K.V., Shur, M.L., Kh Strelets, M. and Travin, A.K., "On the differences in noise predictions based on solid and permeable surface Ffowcs Williams–Hawkings integral solutions." *International Journal of Aeroacoustics* 18, no. 6-7 (2019): 621-646.

[54] "How Joby built a super-quiet electric air taxi." https://www.fastcompany.com/90660149/joby-kitty-hawk-volocopter-air-taxis-noise (accessed 9/12/2022).

[55] Brooks, T.F., Pope, D.S. and Marcolini, M.A., *Airfoil self-noise and prediction*. No. L-16528. 1989.

[56] Schmitz, F.H. and Sim, B.W.C., "Acoustic Phasing, Directionality and Amplification Effects of Helicopter Blade-Vortex Interactions." *Journal of the American Helicopter Society* 46, no. 4 (2001): 273-282.

[57] Coleman, D., Halder, A., Saemi, F., Runco, C., Denton, H., Lee, B. and Benedict, M., "Development of "Aria", a compact, ultra-quiet personal electric helicopter." In *Proc. 77th Annual Vertical Flight Society Forum and Technology Display, FORUM*, pp. 10-14. 2021.

[58] Lakshminarayan, V.K. and Baeder, J.D., "High-resolution computational investigation of trimmed coaxial rotor aerodynamics in hover." *Journal of the American Helicopter Society* 54, no. 4 (2009):

42008-42008.

[59] Block, P.J.W., "Noise radiation patterns of counter-rotation and unsteadily loaded single-rotation propellers." *Journal of Aircraft* 22, no. 9 (1985): 776-783.

[60] Johnston, R.T. and Sullivan, J.P., "Unsteady wing surface pressures in the wake of a propeller." *Journal of Aircraft* 30, no. 5 (1993): 644-651.

[61] Brooks, T.F., Marcolini, M.A. and Pope, D.S., "Main rotor broadband noise study in the DNW." *Journal of the American Helicopter Society* 34, no. 2 (1989): 3-12.

[62] Glegg, S.A., Devenport, W.J., Wittmer, K.S. and Pope, D.S., "Broadband helicopter noise generated by blade wake interactions." *Journal of the American Helicopter Society* 44, no. 4 (1999): 293-301.

[63] Drela, M., "XFOIL: An analysis and design system for low Reynolds number airfoils." In *Low Reynolds Number Aerodynamics: Proceedings of the Conference Notre Dame, Indiana, USA, 5–7 June 1989*, pp. 1-12. Springer Berlin Heidelberg, 1989.

[64] McDonald, R.A. and Gloudemans, J.R., "Open vehicle sketch pad: An open source parametric geometry and analysis tool for conceptual aircraft design." In *AIAA SciTech 2022 Forum*, p. 0004. 2022.

[65] "Release OpenVSP_3.8.1: OpenVSP Version 3.8.1 · OpenVSP/OpenVSP," *GitHub*. https://github.com/OpenVSP/OpenVSP/releases/tag/OpenVSP_3.8.1 (accessed 9/28/2022).

[66] Konzel, N.B. and Greenwood, E., "Ground-based acoustic measurements of small multirotor aircraft." In *Vertical Flight Society 78th Annual Forum & Technology Display, Fort Worth, TX*, pp. 10-12. 2022.

[67] Olson, E.D., "Multi-Disciplinary, Multi-Fidelity Discrete Data Transfer Using Degenerate Geometry Forms." In *17th AIAA/ISSMO Multidisciplinary Analysis and Optimization Conference*, p. 3208. 2016.

[68] Pujol, J., "The solution of nonlinear inverse problems and the Levenberg-Marquardt method." *Geophysics* 72, no. 4 (2007): W1-W16.

[69] Weitsman, D., "Theoretical and experimental study of the effects of cyclic pitch variations on rotor noise." (2022).

[70] Moré, J.J., "The Levenberg-Marquardt algorithm: implementation and theory." In *Numerical Analysis: Proceedings of the Biennial Conference Held at Dundee, June 28–July 1, 1977*, pp. 105-116. Berlin, Heidelberg: Springer Berlin Heidelberg, 2006.

[71] Botre, M., *Rotorcraft noise prediction system validation and analysis for generating noise abatement procedures*. The Pennsylvania State University, 2020.

[72] Hennes, C., Lopes, L. and Shirey, J., "PSUWOPWOP user's manual." *The Pennsylvania State University, University Park, PA* (2009).

[73] Pegg, R.J., *A summary and evaluation of semi-empirical methods for the prediction of helicopter rotor noise*. No. NASA-TM-80200. 1979.

[74] Mukherjee, B., "A Preliminary Investigation of Propeller-Wing Interaction Noise for eVTOL Aircraft." (2021).

[75] Schmitz, F.H., Aggarwal, H.R. and Boxwell, D.A., "Prediction measurement of a low-frequency harmonic noise of hovering model helicopter rotor." *Journal of aircraft* 37, no. 5 (2000): 786-795.

[76] Pettingill, N.A., Zawodny, N.S., Thurman, C. and Lopes, L.V., "Acoustic and performance characteristics of an ideally twisted rotor in hover." In *AIAA Scitech 2021 Forum*, p. 1928. 2021.

[77] Pettingill, N.A. and Zawodny, N.S., *Ideally Twisted Rotor Testing and Predictions*. No. NF1676L-36114. 2020.

[78] Pettingill, N.A. and Zawodny, N.S., "Identification and prediction of broadband noise for a small quadcopter." In *75th Annual Forum & Technology Display*. 2019.

[79] M. G. | March 03 and 2015, "Sikorsky S-76D begins service with Japan Coast Guard," *Aerospace Manufacturing and Design*. https://www.aerospacemanufacturinganddesign.com/news/sikorsky-s76d-helicopter-japan-service-030315/ (accessed Feb. 23, 2023).

[80] Russo, M., Kraljević, L., Stella, M. and Sikora, M., "Acoustic performance analysis of anechoic chambers based on ISO 3745 and ISO 26101: standards comparison and performance analysis of the anechoic chamber at the University of Split." In *Proc. Euronoise*, pp. 1-6. 2018.

[81] Smith, B., Niemiec, R. and Gandhi, F. "A comparison of multicopter noise characteristics with increasing number of rotors." In *76th Annual Forum of the Vertical Flight Society, Virtual*. 2020.

[82] Pascioni, K.A., Rizzi, S.A. and Schiller, N., "Noise reduction potential of phase control for distributed propulsion vehicles." In *AIAA Scitech 2019 Forum*, p. 1069. 2019.